Journal of Materials Chemistry A

ROYAL SOCIETY OF CHEMISTRY

PERSPECTIVE

View Article Online
View Journal | View Issue

Cite this: J. Mater. Chem. A, 2021, 9, 18818

Engineering plasmonic semiconductors for enhanced photocatalysis

Juan Li, [a] Zaizhu Lou *[ab] and Baojun Li*[a]

Localized surface plasmon resonance (LSPR) is an intriguing phenomenon induced by the collective oscillations of free carriers with incident light, and has attracted considerable interest for the plasmon-enhanced photocatalysis. Since the first report of plasmonic photocatalysis in 2009, various materials of metals/semiconductors, bimetals and semiconductors have been reported as active plasmonic photocatalysts. With low-cost and abundant reserves, plasmonic semiconductors are promising candidates for photocatalysis as substitutes for high-cost and rare noble metals. Various plasmonic semiconductors have been explored for photocatalytic chemical reactions such as hydrogen generation, CO_2 reduction, and organic synthesis because of the strong LSPR in visible and near-infrared (Vis-NIR) regions. Moreover, plasmonic semiconductors with both electronic structures of the intrinsic band and LSPR property allow for broad absorption in the UV-Vis-NIR region and are ideal materials for solar energy conversion. However, there still remain obscure problems such as differences between plasmonic semiconductors and metals, LSPR-mediated photochemical and physical processes, as well as a detailed mechanism of LSPR-enhanced photocatalysis over plasmonic semiconductors. In this perspective, we summarize the recent development of plasmonic semiconductors and their promising applicability in photocatalysis. We also highlight and provide an outlook on the advancing research regarding strategies to construct LSPR on semiconductors for high-efficient photocatalysis, including (1) decreasing the thickness of depletion layers, (2) constructing plasmonic p–n heterostructures, (3) anisotropic LSPR on semiconductors and (4) mechanism study on p-type plasmonic semiconductor for photocatalysis.

Received 29th May 2021
Accepted 26th July 2021

DOI: 10.1039/d1ta04541e

rsc.li/materials-a

[a]Institute of Nanophotonics, Jinan University, Guangzhou, 511443, China. E-mail: zzlou@jnu.edu.cn; baojunli@jnu.edu.cn

[b]State Key Laboratory for Crystal Materials, Shandong University, Jinan, 250100, China

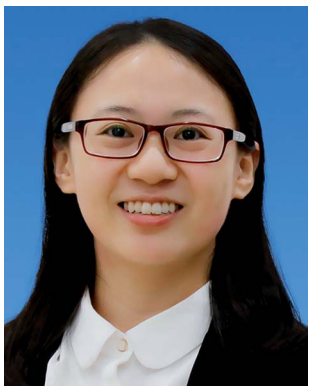

Juan Li received the PhD degree from Sun Yat-Sen University, Guangzhou, China, in 2018. After that, she joined in Jinan University, Guangzhou, China, and currently, she works as an Associate Professor of optical engineering in Institute of Nanophotonics. Her research focuses on the fabrication and functionalization of plasmonic nanostructures and their applications in nanophotonics and energy conversion.

Zaizhu Lou is a professor of materials science and optical engineering at Jinan University. He obtained PhD in materials science under the guidance of Baibiao Huang from Shandong University at 2014. After the Japan Society for the Promotion of Science (JSPS) Supported Research with Tetsuro Majima at Osaka University, he joined Jinan University in 2017. His research interests are in the field of metals or semiconductors with surface plasmon resonance for hot carrier generation, transfer and recombination, and their applications for photocatalytic hydrogen generation and CO_2 reduction. He received funds from Distinguished Young Scholars and Young Pearl River Scholar from the Government of Guangdong Province.

1. Introduction

Localized surface plasmon resonance (LSPR) is an intriguing phenomenon that occurs due to free carrier oscillation of nanoparticles (NPs) with incident light,[1–3] and has been widely applied in various fields including optical information,[4,5] biosensor,[6,7] cancer therapy[8,9] and solar energy conversion.[10,11] Especially, LSPR-enhanced photocatalysis has attracted great attention and considerable efforts have been devoted to the development of plasmonic photocatalysts. In 2008, Awazu *et al.* first reported $Ag/SiO_2/TiO_2$ composites for plasmon-enhanced photocatalysis and pioneered the concept of "plasmonic photocatalysts".[12] Since then, various metal/semiconductor composites including Ag@AgX (X = Cl, Br and I), Au/TiO_2, and Au/CdSe have been reported as plasmonic photocatalysts for water splitting, hydrogen evolution and pollution degradation, respectively.[13–19] Owing to the LSPR effect, plasmonic metals can transfer solar energy to adjacent semiconductors to drive a chemical reaction.[20–23] Intriguingly, apart from enhancing the photoresponse of semiconductors, plasmonic NPs can also excite hot carrier generation, which has been demonstrated to play a dominant role in driving the catalytic reaction.[24–26] However, due to the fast recombination (~100 fs), these active hot carriers suffer from low utilization efficiency for photocatalysis.[27–29] Considering fast charge transfer between metallic parts, bimetallic/multimetallic NPs were expected to promote the separation of hot carriers for enhanced photocatalysis. In 2014, Majima *et al.* synthesized bimetallic Pt–Au NRs, which enable fast hot electrons transfer from Au to Pt, boosting photocatalytic hydrogen generation.[30] Similar phenomena were also observed in other metallic photocatalysts including Pd–Au NRs, and Pt–Au nanoprism/nanodisks.[31–35] Although plasmonic metals display favorable advantages over traditional semiconductors, high cost and rare reserve largely limit their large-scale commercial applications in photocatalysis. Moreover, with the absence of surfactant, pure metal NPs easily aggregate, leading to damping LSPR and poor photocatalytic efficiency.

Recently, various doped semiconductors with high free carriers density have also exhibited the LSPR effect and generated much attention for their great potential in various fields as promising substitutes of noble metals.[36–41] In contrast to metals, the LSPR of semiconductors could be tailored by changing stoichiometric compositions, dopant concentration and phase transitions.[36] In 2014, Yamashita *et al.* reported molybdenum oxides (MoO_{3-x}) with abundant oxygen vacancies as plasmonic photocatalyst for plasmon-enhanced hydrogen generation from ammonia borane under visible light irradiation.[42] Similar phenomena were demonstrated in hydrogen-doped molybdenum oxide (H_xMoO_3),[43] Pd–MoO_{3-x} (ref. 44) and $Mo_xW_{1-x}O_{3-y}$ (ref. 45) with the LSPR effect. In 2015, Xue *et al.* reported plasmonic tungsten oxides (WO_{3-x} and Pd–WO_{3-x}) for LSPR-enhanced photocatalytic activity in ammonia borane decomposition and the Suzuki coupling reaction.[46,47] However, different from the photocatalytic hydrogen generation from water splitting, enhanced activity in organic reactions and ammonia borane degradation can be attributed to the photothermal effect. To further confirm the photocatalysis of plasmonic semiconductors for water splitting, Zhang *et al.* constructed plasmonic heterostructure $W_{18}O_{49}$/g-C_3N_4, in which plasmon-induced hot electrons on $W_{18}O_{49}$ are transferred to CB of g-C_3N_4 for hydrogen generation under NIR-irradiation.[48] However, oxygen vacancies of WO_{3-x} and MoO_{3-x} are easily removed in oxygen and aqueous solution leading to unstable LSPR. Lou *et al.* proposed the strategy of electron injection to maintain the LSPR of oxygen vacancy-doped WO_{3-x}, and several heterostructures of CdS/WO_{3-x},[49] TiO_2/WO_{3-x} (ref. 50) and MoS_2/MoO_{3-x} (ref. 51) have been constructed to prove its feasibility. By single-particle PL study, the photoelectrons generated in the semiconductor are demonstrated to be injected into the CB of plasmonic semiconductor, increasing the free carrier density to stabilize LSPR.[49–51] Although, various plasmonic semiconductors and heterostructures have been developed for plasmon-enhanced photocatalysis. Few studies were focused on the detailed mechanism of LSPR and the generation of hot carriers for photocatalysis. In this perspective, we summarize the recent literature and provide an outlook on the development of plasmonic semiconductors for photocatalysis, divided into three parts: (i) localized surface plasmon resonance on semiconductors; (ii) plasmonic semiconductors for photocatalysis and mechanism; (iii) conclusions and outlook.

Baojun Li received his PhD from Xi'an Jiaotong University in China in 1998. After that, he worked at Fudan University in Shanghai, China, as a Postdoctoral Fellow till 2000. From 2000 to 2002, he worked at Singapore-MIT Alliance and National University of Singapore, first as a Postdoctoral Fellow and then as a Research Fellow. From April to October 2002, he worked at Institute of Materials Research and Engineering in Singapore as a Research Fellow. In 2002, he joined Sun Yat-Sen University in China as a full Professor and served as a Director for Research Laboratory for Optoelectronic Integration in the State Key Laboratory of Optoelectronic Materials and Technologies. From May to November 2009, he worked at the University of Oxford as a senior visiting scholar. Then, he came back to Sun Yat-Sen University as a Cheung Kong Scholar Distinguished Professor and served as a Dean of School of Physics and Engineering. In July 2016, he moved to Jinan University in Guangzhou, China, where he founded Institute of Nanophotonics and currently serves as a Director.

2. Localized surface plasmon resonance on semiconductors

2.1 LSPR dependent on free carrier density of semiconductor

Localized surface plasmon resonance (LSPR) in both metal and semiconductors occur during free carrier oscillation with incident light (Fig. 1).

The physical basis of interaction between the free carriers of materials and the incident light can be described using Maxwell equations. The interaction extent is defined by a complex dielectric function and LSPR phenomenon often exhibited in conductive materials with high free carrier density based on the Drude–Lorentz model as follows:[52,53]

$$\varepsilon_p(\omega) = \varepsilon_1(\omega) + i\varepsilon_2(\omega) \quad (1)$$

$$\varepsilon_1 = \varepsilon_\infty - \frac{{\omega_p}^2}{\omega^2 + \gamma^2} \quad (2)$$

$$\varepsilon_2 = \frac{{\omega_p}^2\gamma}{\omega(\omega + \gamma^2)} \quad (3)$$

where is a dielectric function of materials, ε_1 and ε_2 are the real and imaginary parts of the dielectric function, respectively, ε_∞ is the high-frequency dielectric constant of materials, γ is the damping constant that represents the scattering of free carriers, and ω_p is the plasma frequency that can be described as,[54]

$$\omega_p = \sqrt{\frac{Ne^2}{m_e\varepsilon_0}} \quad (4)$$

where N is the density of free carrier (electron or holes), m_e is the effective mass of carriers. It can be found that ω_p is proportional to the square root of N. As shown in Fig. 2, noble metals (Ag or Au) with a high free electron density of 10^{22} to 10^{23} cm^{-3} exhibit LSPR in the Vis-NIR region. For doped semiconductors, the free-carrier density (N) is around 10^{16} to 10^{21} cm^{-3} and LSPR frequency localizes in NIR to THz regions.[55] As N increases, LSPR frequency has a shift toward low energy region. Ultra-pure Si with N of 2–4 $\times$ 10^{19} cm^{-3} exhibits LSPR in the microwave region.[56]

Various semiconductors with high N value have been explored as plasmonic materials including doped metal oxides (WO_3, In_2O_3, Bi_2O_3, *etc.*),[57–62] metal chalcogenides (CuS, CuSe, HgS, *etc.*),[63–66] II–V compounds and group IV elements (Si, TiN, InN, *etc.*).[56,67–70] The extinction spectra of some plasmonic semiconductors have been summarized in Fig. 3, and most doped semiconductors show LSPR in NIR and mid-NIR regions. To date, plasmonic semiconductors have been demonstrated as promising substitutes for plasmonic metals for enhanced SERS,[71] photoluminescence[72] and photocatalysis.[73]

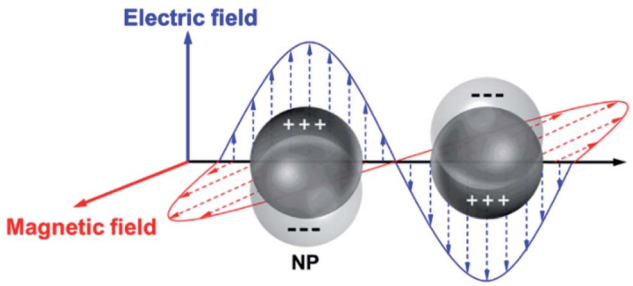

Fig. 1 Schematic of LSPR in NPs.

Different from electron oscillation of plasmonic metals, LSPR of semiconductors can be caused by electrons in CB or holes in VB, which are labeled as n-type and p-type plasmonic semiconductors, respectively. Among them, oxygen-vacancy doped n-type semiconductors of WO_{3-x},[46] MoO_{3-x} (ref. 42) and cation-vacancy doped p-type chalcogenides[74,75] have attracted much attention with LSPR in the Vis-NIR region. In the case of WO_{3-x}, various samples with tunable free carrier density including $W_{18}O_{49}$ ($WO_{2.72}$),[76] W_5O_{14} ($WO_{2.8}$),[77] $W_{24}O_{68}$ ($WO_{2.83}$)[78] and $W_{20}O_{58}$ ($WO_{2.9}$)[79] are obtained by controlling oxygen-deficient stoichiometries. Alivisatos *et al.* synthesized $WO_{2.83}$ nanorods by hot injection reaction in oleic acid/trioctylamine mixture, and its N value was estimated to be 6.3 $\times$ 10^{21} cm^{-3} based on the stoichiometric ratio of oxygen vacancies.[80] The simulated LSPR wavelength of $WO_{2.83}$ nanorods is 860 nm by Mie–Gans theory, consisting of an experimental value of 900 nm, further demonstrating its LSPR feature. More recently, Sardar *et al.* reported WO_{3-x} ($x \approx 0.55$–1.03) nanoplates with ~3 tungsten–oxygen layers thick (~1 nm) (Fig. 4a), and the N value was calculated to be 4.13 $\times$ 10^{22} cm^{-3} using Drude–Lorentz model combining experimental LSPR peak value of 1470 nm (Fig. 4d).[81] Strong LSPR was also observed on mesoporous $WO_{2.83}$ (Fig. 4b and e) and $W_{18}O_{49}$ nanowires (Fig. 4c and f). Besides, H^+ and alkali ions such as Li^+, Na^+, and K^+ can be inserted into the lattices of tungsten oxide crystals, causing an increase of N to support strong LSPR.[36] Ye *et al.* reported H_x-WO_{3-x} with N of 5.04 $\times$ 10^{21} cm^{-3} synthesized by electrical chemical reduction using Fe and Cu foils in HCl solution, which exhibited tunable LSPR in the 500–1500 nm region.[82] Another mostly reported oxygen vacancy doped n-type plasmonic semiconductor is nonstoichiometric MoO_{3-x}. MoO_3 is a semiconductor with a band gap of 3.05 eV. As oxygen atoms are removed from crystal lattices, Mo(VI) around oxygen vacancy captures one electron to become Mo(V), resulting in an enhanced N for LSPR. Tang *et al.* synthesized sub-stoichiometry MoO_{3-x} nanodots (Fig. 4g) *via* chemical oxidation of bulk MoS_2 and subsequent reduction procedure using different reducing agents. The calculated N is around 10^{21} cm^{-3} for tunable LSPR in 800–900 nm, and the LSPR wavelength has a red shift with increasing concentration of reduction reagent during synthesis of MoO_{3-x} (Fig. 4h and i).[83] Cheng *et al.* studied hydrogen-doped MoO_{3-x} by loading Pd on MoO_3 as a catalyst to promote hydrogen insert crystal lattices. By changing the temperature during H_2 reduction, the LSPR wavelength of obtained MoO_{3-x} can be tuned from 565 to 660 nm and the corresponding N values are estimated as 3.1 $\times$ 10^{21} to 5.8 $\times$ 10^{21} cm^{-3} by the Drude model.[43]

The cation vacancy doped copper chalcogenides with free holes on VB belongs to p-type plasmonic semiconductors. Feldmann *et al.* synthesized copper chalcogenide nanocrystals

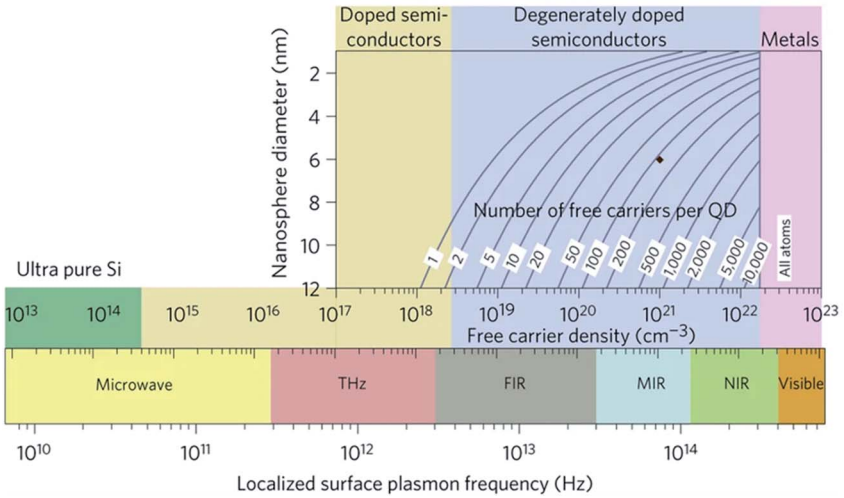

Fig. 2 Plasmon frequency dependence on the free carrier density of metals and semiconductors with various sizes. Reproduced with permission.[55] Copyright 2011, Nature Publishing Group.

(NCs) of $Cu_{2-x}S$, $Cu_{2-x}Se$ and $Cu_{2-x}Te$ ($x > 0$) with tunable LSPR depending on x values (Fig. 5a–c), and N values extracted from LSPR frequency were 1.4×10^{21}, 3×10^{21} and 5×10^{21} cm^{-3} for $Cu_{1.97}S$, $Cu_{1.8}Se$ and $Cu_{1.4}Te$, respectively.[84] Free carrier densities of rhombohedral $Cu_{1.77}S$, $Cu_{1.63}S$, $Cu_{1.43}S$ and hexagonal $Cu_{1.14}S$ NCs with LSPR energy of 1.06, 1.11, 1.25 and 1.09 eV were 4.7×10^{21}, 4.98×10^{21}, 5.99×10^{21} and 6.08×10^{21} cm^{-3}, respectively, calculated using the Mie theory.[85] Hole density on VB of $Cu_{2-x}S$ could be modulated by electron injection from organic polymers (Fig. 5d and e) to obtain "off" or "on" LSPR in the 1000–1500 nm region.[86] The carrier density of some semiconductors with LSPR from the literature is summarized in Table 1.

2.2 Other parameters influencing LSPR of semiconductors

Similar to metal NPs, other parameters including morphology and size also affect the LSPR feature of semiconductors apart from free carrier density. The Mie solution to Maxwell's

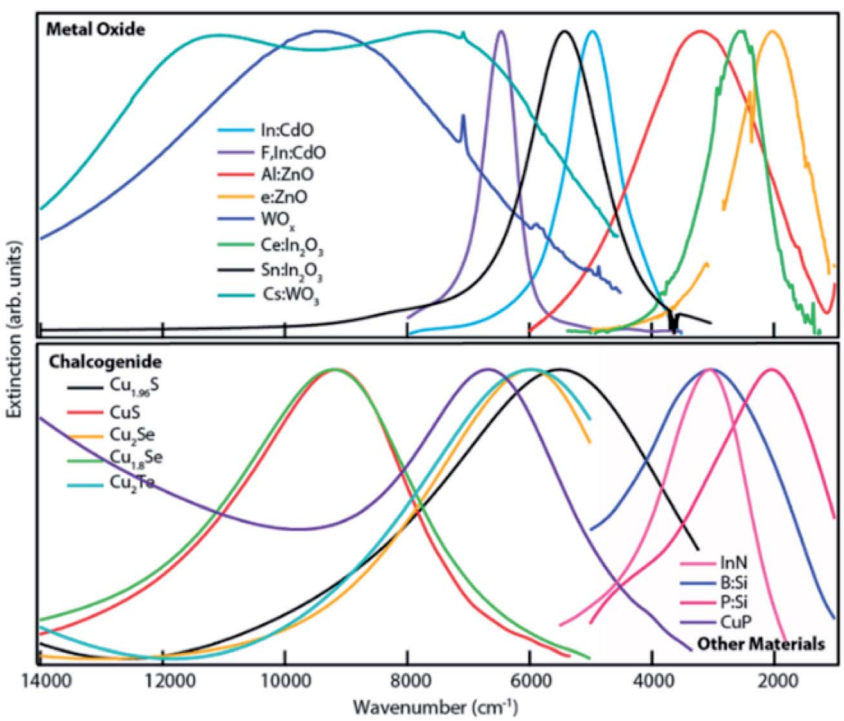

Fig. 3 LSPR spectra of some reported plasmonic semiconductors. Reproduced with permission from ref. 36. Copyright 2018, American Chemical Society.

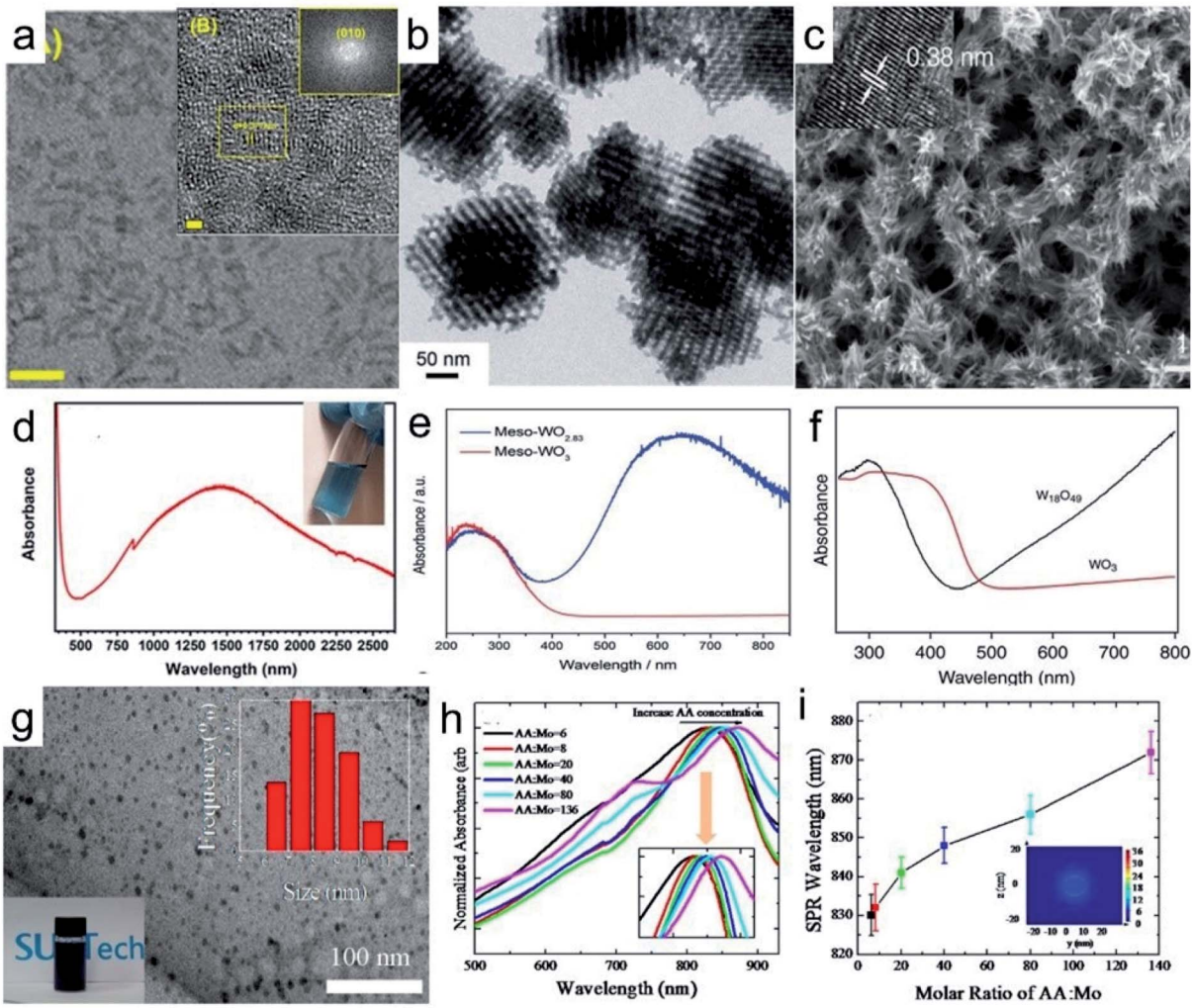

Fig. 4 TEM images of WO_{3-x} nanoplates (a) and ordered mesoporous $WO_{2.83}$ (b), and SEM image of $W_{18}O_{49}$ (c), and their LSPR spectra (d–f). (a and d) Reproduced with permission from ref. 81. Copyright 2020, American Chemical Society. (b and e) Reproduced with permission from ref. 78. Copyright 2018, The Royal Society of Chemistry. (c and f) Reproduced with permission from ref. 76. Copyright 2015, Nature Publishing Group. TEM image of MoO_{3-x} nanodots (g) and the redshift of LSPR wavelength (h and i) with increasing of the reduction reagent. Reproduced with permission from ref. 83. Copyright 2017, American Chemical Society.

equations described the absorption and scattering of spherical NPs under incident light and the extinction cross-section (σ_{ext}) is the sum ($\sigma_{ext} = \sigma_{abs} + \sigma_{sca}$) of the absorption cross-section (σ_{abs}) and scattering cross-section (σ_{sca}). For metal NPs with a size smaller than light wavelength, the Mie solution is represented as eqn (5) and (6) according to Gans theory:[87,88]

$$\sigma_{abs} = \frac{2\pi V}{3\lambda}\varepsilon_m^{\frac{3}{2}}\sum_{j=1}^{3}\frac{\left(\frac{1}{P_j^2}\right)\varepsilon_2}{\left(\varepsilon_1 + \frac{(1-P_j)\varepsilon_m}{P_j}\right)^2 + \varepsilon_2^2} \quad (5)$$

$$\sigma_{sca} = \frac{8\pi^3 V^2}{9\lambda^4}\varepsilon_m^2\sum_{j=1}^{3}\frac{1}{P_j^2}\frac{(\varepsilon_1-\varepsilon_m)^2 + \varepsilon_2^2}{\left(\varepsilon_1 + \frac{(1-P_j)\varepsilon_m}{P_j}\right)^2 + \varepsilon_2^2} \quad (6)$$

where ε_1 and ε_2 are the real and imaginary parts of the complex dielectric function of NPs, respectively, ε_m is the dielectric function of the surrounding medium, V is the NPs volume, λ represents the incident light wavelength, and P_j ($j = 1, 2, 3$) are depolarization factors for three axes of NPs that depend on the aspect ratio. It is clear that all parameters of size, shape, composition and surrounding medium determine LSPR of metal NPs, which are characteristics of LSPR and fundamental of the plasmonic sensor and detector.

For plasmonic semiconductors, LSPR frequency is mainly tuned by controlling doping and carrier density but is also affected by the anisotropic morphologies. Tao *et al.* studied the influence of anisotropic shapes on the LSPR of $Cu_{2-x}S$ nanodisks and near-field LSPR coupling within nanodisk assemblies.[89,90] Milliron *et al.* synthesized plasmonic Cs_xWO_3 with three distinct shapes of hexagonal prisms, truncated cubes and pseudospheres, demonstrating the shape dependence of LSPR features. Two obvious peaks at 860 and 1602 nm assigned to different LSPR modes are observed for hexagonal prism while

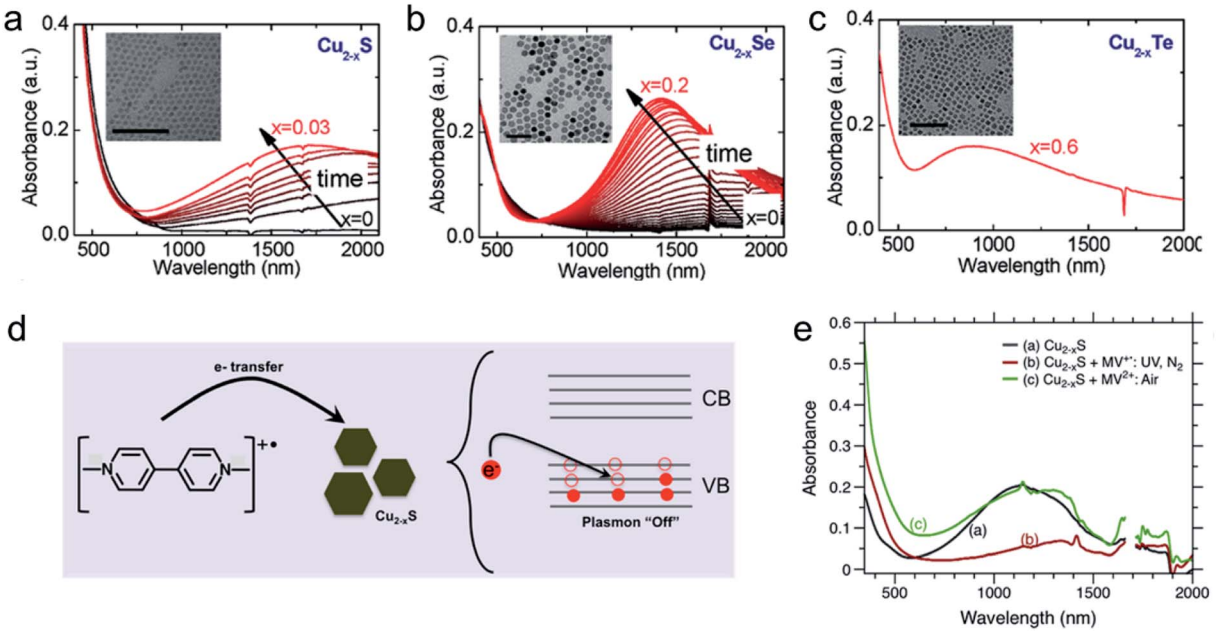

Fig. 5 LSPR spectra and TEM images of $Cu_{2-x}S$ ($x = 0$–0.03, a), $Cu_{2-x}Se$ ($x = 0$–0.2, b) and $Cu_{2-x}Te$ ($x = 0.6$, c). Reproduced with permission from ref. 84. Copyright 2011, American Chemical Society. Schematic diagram (d) of photoinduced electron transfer to tune LSPR of plasmonic $Cu_{2-x}S$ and the shift of their LSPR spectra (e). Reproduced with permission from ref. 86. Copyright 2016, American Chemical Society.

there is only one peak for pseudosphere Cs_xWO_3.[91] They also investigated the influence of anisotropic shape and crystalline structure on LSPR of hexagonal Cs-doped WO_3 NCs, and a reasonable illustration was given by the Drude model considering the directions in crystal structures,[92]

$$\vec{\varepsilon}_D(\omega) = \vec{\varepsilon}_\infty(\omega) - \frac{\vec{\omega}_p^{\,2}}{\omega^2 - \omega\vec{\gamma}} \quad (7)$$

$$\vec{\omega}_p = \sqrt{\frac{Ne^2}{\varepsilon_0 \vec{m}_e}} \quad (8)$$

Table 1 Carrier density of some semiconductors with LSPR[a]

Samples	λ_{LSPR} (nm)	Carrier density (cm^{-3})	Samples	λ_{LSPR} (nm)	Carrier density (cm^{-3})
$WO_{2.17}$	1468	3.36×10^{22} (ref. 81)	In_2O_3	2670	0.69×10^{21} (ref. 137)
$WO_{2.37}$	1596	2.53×10^{22} (ref. 81)	$Sn:In_2O_3$ (0.5%)	2600	0.74×10^{21} (ref. 137)
$WO_{2.02}$	1346	3.95×10^{22} (ref. 81)	$Sn:In_2O_3$ (1%)	2305	0.94×10^{21} (ref. 137)
$WO_{2.34}$	984	2.68×10^{22} (ref. 81)	$Sn:In_2O_3$ (3%)	2088	1.15×10^{21} (ref. 137)
$WO_{2.45}$	1535	2.23×10^{22} (ref. 81)	$Sn:In_2O_3$ (4%)	1974	1.17×10^{21} (ref. 137)
$WO_{2.30}$	1522	2.82×10^{22} (ref. 81)	$Sn:In_2O_3$ (5%)	1917	1.25×10^{21} (ref. 137)
$WO_{2.03}$	1360	3.91×10^{22} (ref. 81)	$Sn:In_2O_3$ (10%)	1707	1.32×10^{21} (ref. 137)
$WO_{1.97}$	1257	4.13×10^{22} (ref. 81)	$Sn:In_2O_3$ (12.5%)	1743	1.26×10^{21} (ref. 137)
MoO_{3-x}	830–872	5.34–5.89×10^{21} (ref. 52)	$Ce:In_2O_3$	3765	2.45×10^{20} (ref. 138)
MoO_{3-x}	750	8.1×10^{21} (ref. 134)	Cr-ITO	1749	1.29×10^{21} (ref. 139)
$Cu_{1.2}S$	1240	2.64×10^{21} (ref. 123)	In:CdO	>2500	0.81–1.33×10^{21} (ref. 140)
$Cu_{1.4}S$	1377	2.50×10^{21} (ref. 123)	Al:ZnO (0.8%)	1310	1.9×10^{20} (ref. 141)
$Cu_{1.75}S$	1530	3.14×10^{21} (ref. 123)	Al:ZnO (1.6%)	730	6.1×10^{20} (ref. 141)
$Cu_{1.94}S$	1441	3.50×10^{21} (ref. 123)	Al:ZnO (3.2%)	610	8.7×10^{20} (ref. 141)
$Cu_{1.62}Se$	1265	4.50×10^{21} (ref. 135)	Sn:ZnO	600	8.69×10^{20} (ref. 142)
$Cu_{1.68}Se$	1180	5.24×10^{21} (ref. 135)	Sn:ZnCdO	880	7.32×10^{20} (ref. 142)
$Cu_{1.65}Se$	1033	6.86×10^{21} (ref. 135)	B:Si NCs	3082	4.3×10^{20} (ref. 143)
$Cu_{1.8}Se$	~1400	3.0×10^{21} (ref. 84)	P:Si NCs	10 235	4.3×10^{19} (ref. 143)
$Cu_{2-x}Se$	1075	3.07×10^{21} (ref. 136)	$Mo:TiO_2$	650	1.61×10^{22} (ref. 144)
$Cu_{1.4}Te$	800–900	5.0×10^{21} (ref. 84)	$Nb:TiO_2$	3300	6.26×10^{20} (ref. 144)
Pd/MoO_{3-x}	565	5.80×10^{21} (ref. 44)	$CaNbO_3$	672	1.62×10^{22} (ref. 73)
Pd/WO_{3-x}	660	3.10×10^{21} (ref. 44)	$SrNbO_3$	688	1.48×10^{22} (ref. 73)
HgS	10 780	1.60×10^{19} (ref. 65)	$BaNbO_3$	711	1.41×10^{22} (ref. 73)

[a] All the carrier densities are calculated using the Drude–Lorentz model.

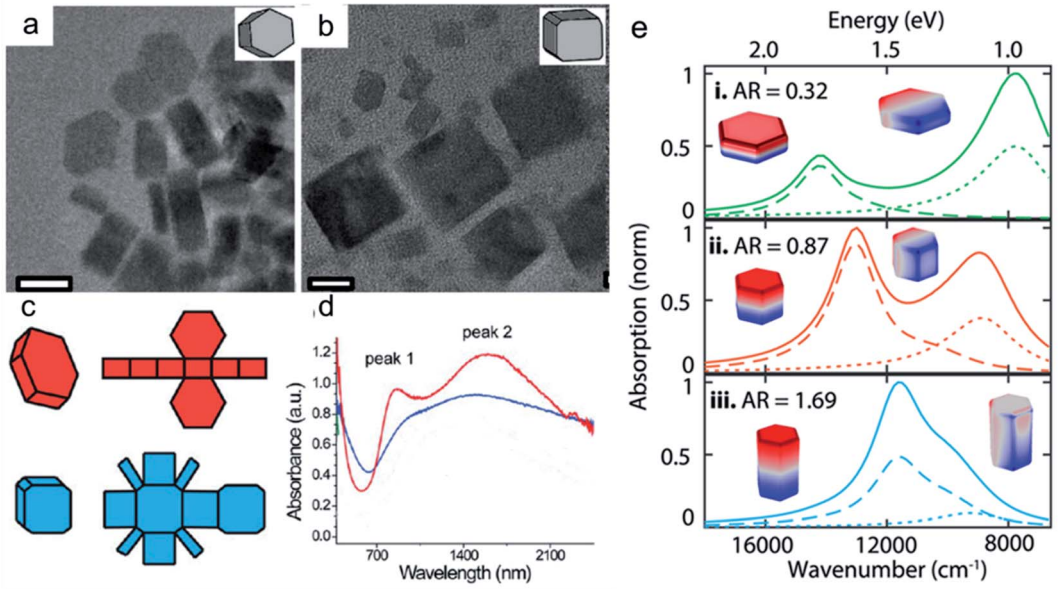

Fig. 6 TEM images of Cs_xWO_3 hexagonal prisms (a) and truncated cubes (b), and illustration of their faceted shapes (c). Absorbance spectra (d) from top to bottom of Cs_xWO_3 hexagonal prisms, truncated cubes, pseudospheres and $WO_{2.72}$ rods, respectively. Reproduced with permission from ref. 91. Copyright 2014, American Chemical Society. (e) Theoretically simulated LSPR spectra for platelet-, iso-prism- and rod-shaped NCs using the anisotropic dielectric function of h-Cs:WO_3. Reproduced with permission from ref. 92. Copyright 2016, American Chemical Society.

Dielectric permittivity ($\vec{\varepsilon}_D$) and bulk plasma frequency ($\vec{\omega}_p$) are determined by the free carrier concentration (N), elementary electronic charge (e), free space permittivity (ε_0), high-frequency permittivity ($\vec{\varepsilon}_\infty$), damping ($\vec{\gamma}$) and electron effective mass ($\vec{m}_e$); the last three of which vary with the direction in crystals with anisotropic structures. In the case of bulk h-Cs_xWO_3, $\vec{m}_e$, $\vec{\varepsilon}_\infty$ and $\vec{\gamma}$ are all strongly dependent on the lattice direction. Specifically, m_e along the c-axis is much lower than that parallel to the basal plane, which results in longitudinal ω_p being 1.5 folds higher than transverse one. The LSPR spectra of anisotropic h-Cs_xWO_3 NCs have been theoretically simulated using the anisotropic dielectric function, as shown in Fig. 6e. As the aspect ratio (AR) of NCs increases, the two LSPR peaks corresponding to the longitudinal and transverse modes shift and come close to each other gradually.

According to eqn (5) and (6), the size of metal NPs is also one parameter influencing the LSPR feature. However, the size changes in semiconductor NCs usually cause the variation of other parameters including doped carrier density, crystalline phase and chemical interface. To investigate the size effect, Xu *et al.* investigated the LSPR of $Cu_{2-x}S$ NCs under a steady-state by tuning the LSPR absorption band to a limiting condition (denoted "pinning" condition).[93] According to the Drude model, for NCs whose size D is comparable to the mean free path of carriers, the LSPR frequency (ω_{sp}) is demonstrated as:[93]

$$\omega_{sp} = \sqrt{\frac{{\omega_p}^2}{1+2\varepsilon_m} - \left(\gamma_b + A\frac{v_F}{D}\right)^2} \quad (9)$$

where γ_b is bulk damping parameter, v_F is Fermi velocity of NCs and A is an empirical constant. Under the pinning condition, $Cu_{2-x}S$ with different sizes have the same copper vacancy density, crystalline phase, similar chemical interface but only different diameters. As the size of NCs increases, the damping parameter γ (effective collision frequency) decreased, leading to the increment of ω_{sp}.[55]

Dielectric function (ε_m) of the surrounding medium is another parameter affecting the LSPR feature of semiconductor NCs, and its sensitivity determines the feasibility as plasmonic sensors. Compared to metals, the LSPR of semiconductor NCs shows lower sensitivity to ε_m, which is mostly determined by the relatively low carrier density on the surface of semiconductors. Milliron *et al.* discussed the presence of a depletion layer near the surface of the semiconductor that has a greatly reduced carrier density, even below the limit required for LSPR properties. As described in Fig. 7a, under an oxidizing surface potential, the conduction-band minimum bends upward near the surface due to the potential gradient of the depletion layer. This band bending leads to a dramatic decrease of free carrier density near the surface with an oxidizing potential, creating an insulating barrier between its plasmonic core and the surroundings (Fig. 7b).[94] This insulating shell reduces the conductivity in NC films, weakens the dipole–dipole interaction between nearby NCs (Fig. 7c), lowers the dielectric sensitivity of LSPR and diminishes the incident electric field enhancement. Due to the existence of an insulating shell, the carrier density of plasmonic semiconductor NCs is mostly calculated by the Drude model instead of experimental measurements. Milliron *et al.* also proposed three methods to tune the depletion effect including electrochemical modulation, chemical surface treatment and intra-NC dopant distribution control.[95]

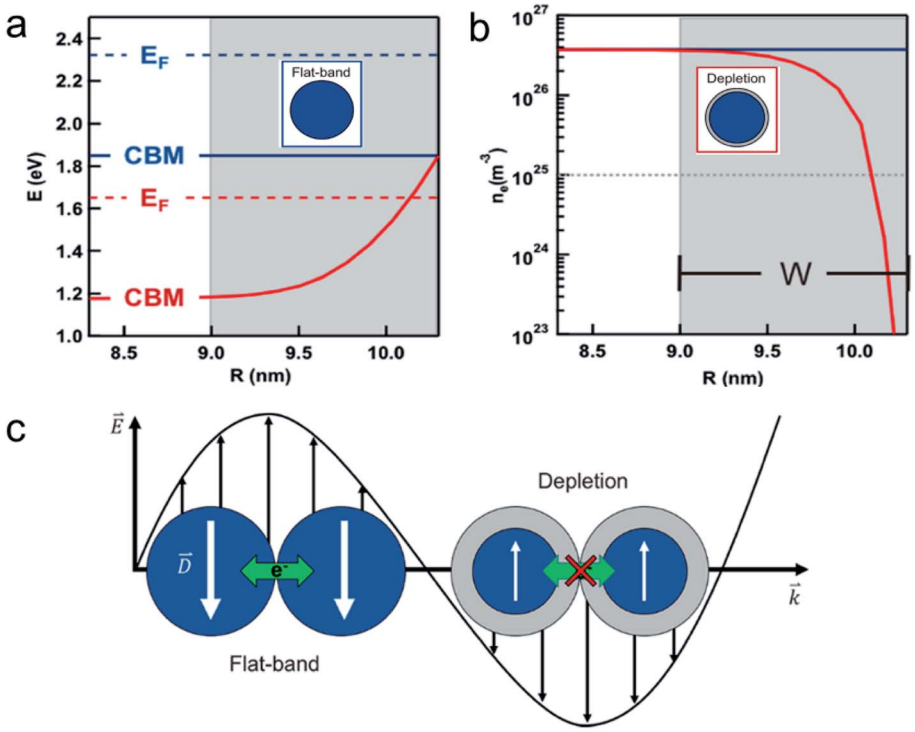

Fig. 7 Simulated conduction-band minimum (CBM) (a) and carrier density (b) in the depletion layer of plasmonic semiconductor NCs. (c) Illustration of weak dipole–dipole interactions between nearby NCs with depletion layers. Reproduced with permission from ref. 95. Copyright 2019, American Chemical Society.

3. Plasmonic semiconductor NCs for photocatalysis and mechanism

3.1 Plasmon-enhanced photocatalysis

Since the photocatalysis on TiO_2 was firstly found by Fujishima *et al.* in 1972, various semiconductor-based photocatalysts have been developed and photocatalysis is expected as one "green" technology to utilize solar energy for solving the dilemma of energy shortage and environmental pollution. Following the development of 'plasmonic photocatalyst', LSPR enhanced photocatalysis has fascinated great attention in past decades. The LSPR enables significant electric field enhancement within nanoscale "hot spots" region around the NP surface, known as near-field enhancement, leading to strong light absorption and enhanced charge-carrier generation. For plasmonic metal–semiconductor composites, three possible energy transfer processes including DET, RET and LEMF are proposed as LSPR-induced charge separation mechanisms, which have been widely reported in other reviews and would not be discussed here.

The excited LSPR undergoes decay by either radiative photon emission or nonradiative relaxation to generate hot carriers (electrons or holes), which play a dominant role in driving the chemical reaction. During the plasmonic photocatalytic process, LSPR-induced hot electrons can be transferred to adjacent nanostructures or directly interact with surface adsorbates to initiate reactions. The extracted hot electrons can activate specific chemical bonds of reactants and modify the reaction pathway to modulate the product selectivity.[26] Moreover, hot electrons enable accelerated desorption of certain surface-adsorbed species, further promoting the catalytic chemical reaction. However, ultrafast measurements have shown that LSPR-excited hot carriers rapidly thermalized in isolated NPs and exhibit an extremely short lifetime, which makes them difficult to be utilized efficiently. Compared to widely studied redox reactions driven by hot electrons, the ones that are driven by hot holes are less explored, mostly due to a much shorter lifetime of hot holes. Therefore, effective separation and collection of plasmonic hot carriers is a difficult and key point for highly efficient chemical conversions. Besides, the hot carriers that do not participate in a reaction could dissipate their electronic energy to lattice vibrations *via* strong electron-phonon scattering, inducing a considerable photothermal effect, which is also favorable for most chemical conversion known as plasmonic photo-thermocatalysis.[96] The plasmonic hot carrier and photothermal effect are crucial features of LSPR, which are mostly investigated to fully understand the mechanisms of LSPR-enhanced photocatalysis and provide guidelines for developing efficient plasmonic photocatalysts.

Recently, semiconductor NCs with LSPR have attracted considerable attention for their low-cost and abundant reserve as promising substitutes in plasmonic noble metals. Compared to semiconductors or metals, plasmonic semiconductors combine the advantages of two materials together on the "one". Those "two" on "one" make plasmonic semiconductors to show a broad light response region from UV-Vis to NIR for efficient

solar energy conversion. To date, various plasmonic semiconductors including doped tungsten oxides, molybdenum oxides and copper chalcogenides have been reported to exhibit promising applicability in plasmon-driven photocatalytic reactions such as water splitting, CO_2 reduction, organic synthesis and pollution decomposition. More recently, several new plasmonic semiconductors such as $Bi_{2-x}O_3$ and Bi_2WO_6 with LSPR in Vis-NIR have also been developed as photocatalysts for CO_2 reduction.[62,97] Details of plasmonic semiconductors developed for photocatalysis are summarized in three parts below.

3.2 Plasmonic MoO_{3-x} and WO_{3-x} for photocatalysis

MoO_3 and WO_3 are well known as electrochromic or photochromic materials in the industry, due to their electron storage ability *via* valence changes of W^{6+}/W^{5+} and Mo^{6+}/Mo^{5+}. Compared to normal doped metal oxides with N below 10^{20}, the carrier density of doped MoO_3 and WO_3 can reach 10^{21} to 10^{22} for strong LSPR in the Vis-NIR region. In 2014, Yamashita *et al.* synthesized MoO_{3-x} nanoplates (Fig. 8a) with abundant oxygen vacancies using the surfactant-free solvothermal method, which exhibited strong and tunable LSPR in the Vis-NIR region (Fig. 8b) for enhanced hydrogen generation from ammonia borane decomposition (Fig. 8c).[42] Pd NPs loaded on MoO_3 can act as a cocatalyst to accelerate the reduction of Mo^{6+} to Mo^{5+} for tunable LSPR and high-active plasmon-enhanced performance for hydrogen generation.[44] Moreover, $Mo_xW_{1-x}O_{3-y}$,[45] high-surface-area MoO_{3-x},[98] ordered mesoporous $WO_{2.83}$,[78] $W_{18}O_{49}$,[46] $W_{18}O_{49}$/TiO_2,[99] $W_{18}O_{49}$/carbon,[100] $NaYF_4$:Yb–Er/$W_{18}O_{49}$ nanowires,[101,102] Ag/$W_{18}O_{49}$ (ref. 103) and Er–Yb:TiO_2/MoO_{3-x} (ref. 104) have been explored as plasmonic photocatalysts to enhance hydrogen generation from ammonia borane. However, the plasmonic enhancement on the degradation of ammonia borane is more like a photothermal-enhanced reaction rather than an improved redox reaction. Actually, due to more positive CB potential as compared to the H^+/H_2 redox potential, tungsten oxide alone cannot be used for photocatalytic hydrogen evolution from water splitting. Meanwhile, LSPR-excited hot electrons on plasmonic NC surface are photocatalytically inert for hydrogen evolution without an active medium. A valid tactic to address these issues is to integrate plasmonic semiconductors with other appropriate active semiconductors for constructing new Z-scheme heterostructures as plasmonic photocatalysts. Dong *et al.* loaded plasmonic $W_{18}O_{49}$ nanograsses onto exfoliated g-C_3N_4 nanosheets as plasmonic heterostructures for full spectrum-driven photocatalytic hydrogen generation from water reduction (Fig. 8d and e), further demonstrating the role of semiconductors LSPR in photocatalysis.[48] The hot electrons excited in $W_{18}O_{49}$ transferred to the CB of neighboring g-C_3N_4 nanosheets for reducing the protons into hydrogen (Fig. 8f). The process of hot electron transfer (HET) is analogous to the DET mechanism that has been proposed to explain LSPR-enhanced photocatalytic activity for traditional plasmonic metal/semiconductor systems. This possible HET mechanism in plasmonic $W_{18}O_{49}$/g-C_3N_4 has also been proposed in other literature.[105]

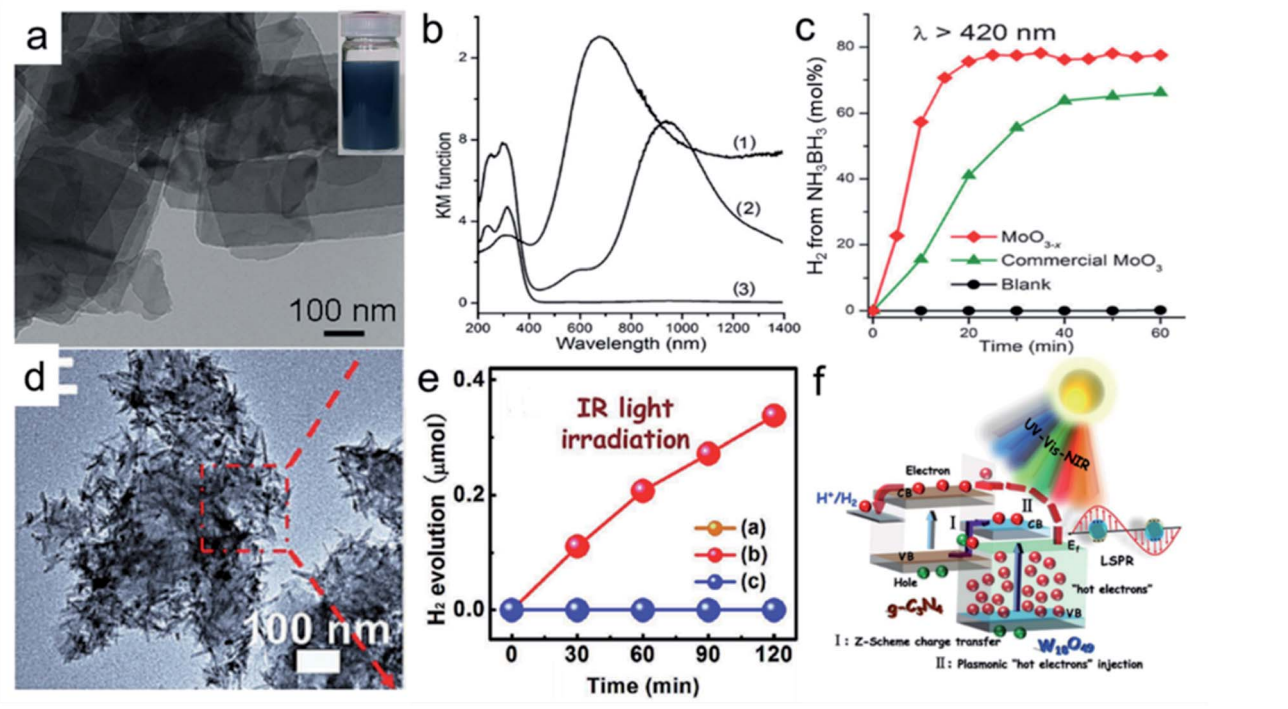

Fig. 8 TEM images of MoO_{3-x} nanoplates (a), their LSPR spectra (b) and plasmon-enhanced hydrogen generation (c) from NH_3BH_3 degradation under visible light irradiation. Reproduced with permission from ref. 42. Copyright 2014, Wiley-VCH. TEM image (d) of $W_{18}O_{49}$/g-C_3N_4 heterostructures, and their photocatalytic hydrogen generation (e) and mechanism (f) under IR light irradiation. Reproduced with permission from ref. 48. Copyright 2017, Wiley-VCH.

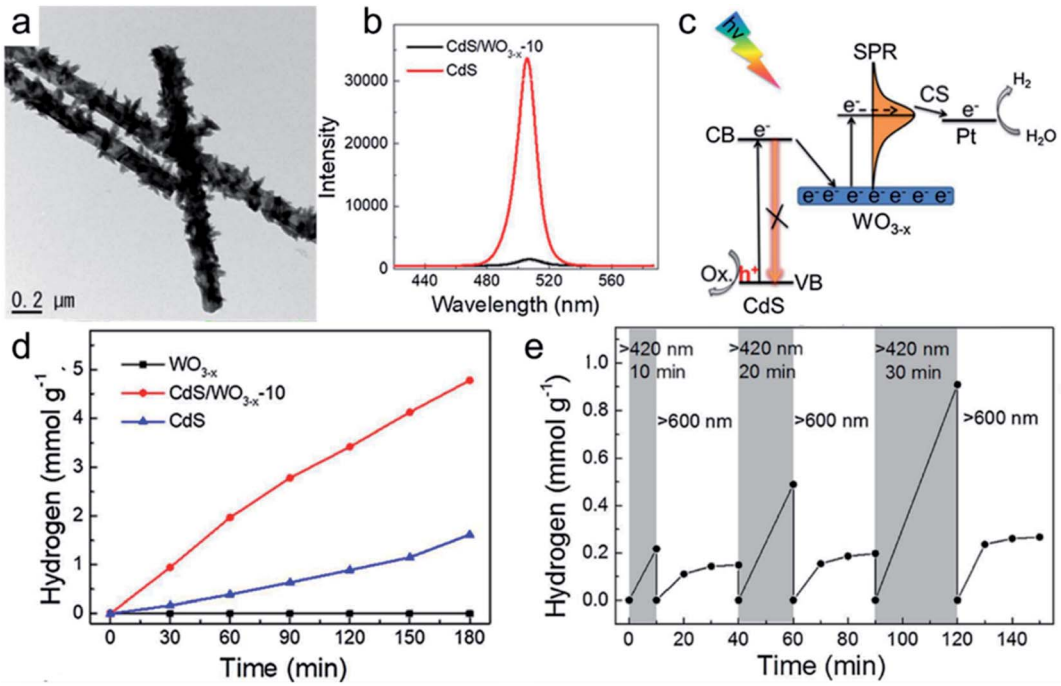

Fig. 9 TEM image (a) of CdS/WO_{3-x} nanowires, PL spectra (b) of CdS/WO_{3-x} and CdS, the photocatalysis mechanism (c) on plasmonic CdS/WO_{3-x}. Photocatalytic hydrogen generation over CdS/WO_{3-x} as catalysts under >420 nm (d) and >600 nm (e) light irradiation. Reproduced with permission from ref. 49. Copyright 2018, Elsevier B.V.

The oxygen vacancies on plasmonic WO_{3-x} and MoO_{3-x} are easily removed in oxygen and the aqueous solution, which leads to the decrease of free carrier density for damping LSPR. The unstable LSPR of oxygen vacancy doped WO_{3-x} and MoO_{3-x} restricts their practical applications in a complex environment as photocatalysts. To solve this issue, Lou *et al.* proposed the concept of electron injection to maintain the LSPR of oxygen-vacancy doped semiconductors. Plasmonic heterostructure of CdS/WO_{3-x} nanowires were synthesized, in which photoelectrons generated in CdS could transfer to the CB of plasmonic WO_{3-x} and increase free electron density for stable LSPR (Fig. 9).[49] The high stability of plasmonic CdS/WO_{3-x} for photocatalytic hydrogen generation in an aqueous solution is demonstrated by repeated reactions after one week. The photoelectron injection from CdS to WO_{3-x} was demonstrated by single-particle PL spectroscopy with 90% quenching efficiency. After the photocatalytic reaction, the color of CdS/WO_{3-x} became dark blue indicating an increase in electron density in WO_{3-x}. As the photoelectron injection is stopped by switching irradiation from >420 nm to >600 nm, hydrogen generation was found to decrease rapidly over WO_{3-x}, further demonstrating the crucial role of electron injection for its stable photocatalysis.

Plasmonic semiconductors have also been employed as effective photocatalysts to facilitate the photoreduction of CO_2 into valuable chemicals such as CO, CH_4, and MeOH, which is akin to killing two birds with one stone in view of mitigating global warming and simultaneously generating alternative energy.[106] In general, photocatalytic CO_2 reduction is a more complicated process than the water-splitting reaction due to the difficulty of CO_2 adsorption and various intermediate reactants. Moreover, CO_2 molecules are highly thermodynamically stable, and the activation of CO_2 requires high energy by conventional methods. Oxygen-vacancy doped semiconductors are considered promising in the field of CO_2 conversion by taking advantage of the LSPR effect and rich active sites. The oxygen vacancies on semiconductors act as high reactive sites to promote the adsorption and activation of CO_2, while the LSPR effect can facilitate strong light absorption and excite hot electron generation for CO_2 reduction. Besides, different adsorption/desorption of reactants on active sites and activation of specific chemical bonds by hot electrons can modify the reaction pathway to modulate products selectivity. Plasmonic heterostructures of TiO_2/WO_{3-x} (ref. 50) and MoS_2/MoO_{3-x} (ref. 51) have been synthesized successfully for photocatalytic CO_2 reduction, and CH_4 and CO were generated as main products, respectively. Efficient photoelectron injection stabilizes the LSPR of semiconductors and boosts continuous hot electron generation for enhanced CO_2 reduction over heterostructures. Different from the HET mechanism of $W_{18}O_{49}$/g-C_3N_4 discussed above, this improved catalytic activity was illustrated by direct hot-electron reaction (DHER) on plasmonic semiconductors. Detailed mechanisms of HET and DHER will be discussed in Section 4.

Due to the intrinsic band and plasmon excitation, plasmonic semiconductors enable broadband light absorption across the full spectrum region. Intriguingly, UV light excited electron transitions from VB to CB maintain the density of the free electrons to stabilize LSPR of oxygen vacancy doped semiconductors, similar to self Z-scheme electronic structures. Lou *et al.* demonstrated this process on plasmonic WO_{3-x} under UV-

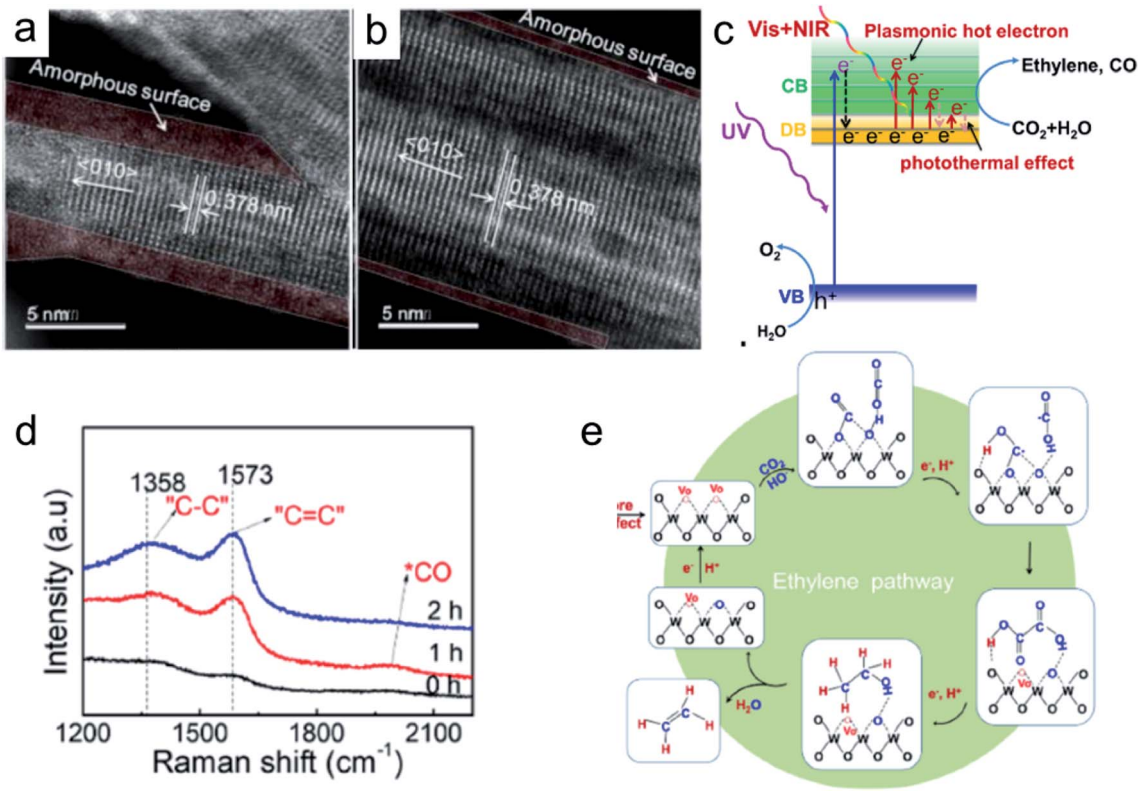

Fig. 10 TEM images of WO_{3-x} nanowires with thick (a) and thin (b) amorphous layers, and their photocatalytic mechanism (c) for CO_2 reduction. Raman spectra (d) and possible ethylene generation pathway (e) over WO_{3-x} nanowires with thin amorphous layer as catalysts during CO_2 photocatalytic reduction. Reproduced with permission from ref. 109. Copyright 2020, Elsevier B.V.

Vis light irradiation, and photoelectron injection from VB boosting the continuous hot electron generation for photocatalytic organic synthesis of aldehyde from ethanol dehydrogenation.[107] Besides, NIR light excited plasmonic photothermal effect contributed to the enhanced catalytic activity and make a big difference to the product selectivity. Under UV-Vis-NIR light irradiation, plasmonic WO_{3-x} with abundant oxygen vacancies selectively yields a remarkable ethylene generation from ethanol dehydration.[108] More oxygen vacancies also promote the C–C coupling reaction and plasmonic WO_{3-x} with high surface oxygen vacancy density achieved selective ethylene generation from CO_2 reduction (Fig. 10).[108,109] More interestingly, the amorphous layers on plasmonic WO_{3-x} surface were demonstrated to play a critical role on catalytic activity, consistent with the effect of the depletion layer on plasmonic semiconductor discussed above. Due to the continuous photoelectron injection, Plasmonic WO_{3-x} with a thin depletion layer has a rapidly increased free carrier density on the surface. It facilitates hot electron generation for CO_2 reduction and carbon coupling reaction, leading to more efficient multi-carbon compounds generation.

Plasmonic semiconductors have displayed remarkable activity in various common photocatalytic reactions. For example, plasmonic $Mo_{1-x}W_xO_{3-y}$ and metal-reduced WO_{3-x} films with tunable LSPR have also been used for efficient photoelectrochemical water splitting with increased photocurrent density,[82,110] attributing to enhanced light absorption, conductivity and charge carrier concentration. The conversion of N_2 to NH_3 is a crucial process in modern agriculture and the chemical industry, which usually requires harsh reaction conditions and high energy input due to the difficulty of activation and dissociation of the nonpolar N≡N bond. Plasmon-assisted solar-driven ammonia synthesis has attracted intensive research interest as the reaction can be performed under mild conditions. Plasmonic MoO_{3-x} nanosheets with oxygen vacancy achieved efficient plasmon-driven N_2 photofixation under Vis-NIR irradiation.[111] The oxygen vacancies on MoO_{3-x} act as rich active sites for N_2 adsorption while plasmon-excited energetic hot electrons with high reductive potential for efficient photochemical N_2 fixation without any other co-catalyst. Moreover, H^+ and alkali ions like Li^+, Na^+, K^+, Rb^+ and Cs^+ were inserted into crystal lattices of WO_3 and MoO_3 to form plasmonic semiconductors as plasmon-driven photocatalysts for environmental purification. Specifically, Cs_xWO_3 displays strong LSPR properties in the NIR region caused by free carrier oscillation. A variety of heterostructures, such as Cs_xWO_3/ZnO,[112] Cs_xWO_3/BiOCl,[113] Cs_xWO_3/TiO_2 (ref. 114) and Cs_xWO_3/g-C_3N_4 (ref. 115) have been constructed as efficient photocatalysts for decompositions of toxic NO gas, organic pollutants (RhB or MB dyes), and volatile organic compounds (HCHO or/and toluene), respectively. Yamashita *et al.* synthesized H_xMoO_3 with tunable LSPR by loading Pd NPs as a catalyst on MoO_3 to

promote intercalation of H atoms into crystal lattices, which displayed LSPR-enhanced catalytic activity toward *p*-nitrophenol reduction.[43]

3.3 Plasmonic copper chalcogenides for photocatalysis

Copper chalcogenides NCs with cationic vacancies as p-type plasmonic semiconductors have also been widely investigated. Their LSPR dependence on free carrier density, anisotropic structures, composition and size are well discussed through experiments and calculations. With broad spectra response in the Vis-NIR region, plasmonic copper chalcogenides $Cu_{2-x}X$ (X = S, Se or Te) have drawn great attention and are considered promising for photocatalytic applications. Polyhedral 26-facet Cu_7S_4 microcages and $Cu_{2-x}Se$ nanospheres were synthesized to exhibit high activities in photodegradation of methylene blue (MB) dyes.[116] $Cu_{1.8}Se/Cu_3Se_2$ composites with efficient charge separation showed enhanced photocatalytic activity in methyl orange degradation under Vis-NIR irradiation.[117] Tian *et al.* reported hierarchical Cu_7S_4–Cu_9S_8 heterostructure hollow cubes with strong plasmonic absorption for enhanced photothermal aerobic oxidation of amines to imines.[118] $Cu_{2-x}Se$ and $Cu_{2-x}S$ were used to modify n-type semiconductors of $Mn_{0.5}Cd_{0.5}S$, $BiVO_4$ and g-C_3N_4, promoting charge separation for enhanced photocatalytic hydrogen generation, antibiotic pollution and RhB degradation, respectively.[119–121] Zhang *et al.* reported $Cu_{2-x}S$/g-C_3N_4 composite with intimate interface contact and S–C bond coupling, which act as an efficient photocatalyst for full solar spectrum-driven CO_2 photoreduction due to efficient charge transfer.[122] Recently, Jiang *et al.* synthesized a range of plasmonic $Cu_{2-x}S$ NCs ($Cu_{1.2}S$, $Cu_{1.4}S$, $Cu_{1.75}S$, and $Cu_{1.94}S$) with tunable LSPR acting as photocatalysts for degradation of MO dyes.[123] $Cu_{1.94}S$ NCs with the highest LSPR energy exhibited the best photocatalytic performance due to Cu vacancy-induced high density of free holes. Millstone *et al.* reported $Cu_{2-x}Se$ as a plasmonic photocatalyst for plasmon-driven dimerization of 4-nitrobenzenethiol to 4,4′-dimercaptoazobenzene with high yield.[124] Chen *et al.* reported plasmonic Pd–$Cu_{2-x}S$ for LSPR-enhanced hydrogen generation from ammonia borane.[125] Controlled growth of CdS–$Cu_{2-x}S$ heteroshells on Au NPs integrated LSPR of Au in the visible region and that of $Cu_{2-x}S$ in NIR region and therefore exhibited improved photocatalytic activity in RhB degradation and photothermal efficiency.[126]

As p-type plasmonic semiconductors, LSPR excitation of $Cu_{2-x}X$ induces hot hole generation and thermal effect, but few reports focused on their detailed mechanism for enhanced photocatalysis. The relative contribution of hot carrier and photothermal effect to photocatalytic performance enhancement has been the subject of intense debate. Recently, Yang *et al.* studied the photophysical process of plasmonic semiconductors using p-type $Cu_{2-x}Se$ NCs as a plasmonic platform and adsorbed rhodamine B (RhB) molecules as both hot carrier acceptor and a local thermometer.[127] By transient absorption spectroscopy, they measured that the adsorbate temperature rises and decays with time constants of 1.4 ± 0.4 and 471 ± 126 ps, respectively, after plasmon excitation of $Cu_{2-x}Se$ at 800 nm. These time constants are on the same time scale as the $Cu_{2-x}Se$ lattice temperature, demonstrating rapid energy transfer from the lattice phonons to the adsorbates. This study provides an insight into the transient heating effect of surface adsorbates on plasmonic NCs and their role in plasmonic photocatalysis. Key photophysical processes of plasmonic photocatalysts and possible heating transfer processes were described in Scheme 1 as following three steps: (i) desorption induced by electronic transition mechanism (DIET); (ii) heat of surface adsorbates by direct thermal equilibrium with the lattice phonon; (iii) heat transfer to the surrounding medium. However, it is still unclear for "hot hole" and its contributions to plasmonic photocatalysis.[127]

3.4 Other plasmonic semiconductors for photocatalysis

Besides the two types of doped semiconductors above, several intrinsic plasmonic semiconductors with LSPR in the visible region have also been developed as plasmonic photocatalysts. Boltasseva *et al.* synthesized TiN@TiO_2 core–shell NPs as plasmon-enhanced photosensitizers for efficient singlet oxygen ($^1O_2$) generation. The possible mechanism of hot carrier-mediated photocatalysis was described as a three-step process: (i) the incoming photon forms an LSPR which decays nonradiatively into hot electrons with efficiency η_{abs}; (ii) a fraction of hot carriers (η_s) is generated by Landau damping at the TiN–TiO_2 interface, with remaining carriers being generated *via*

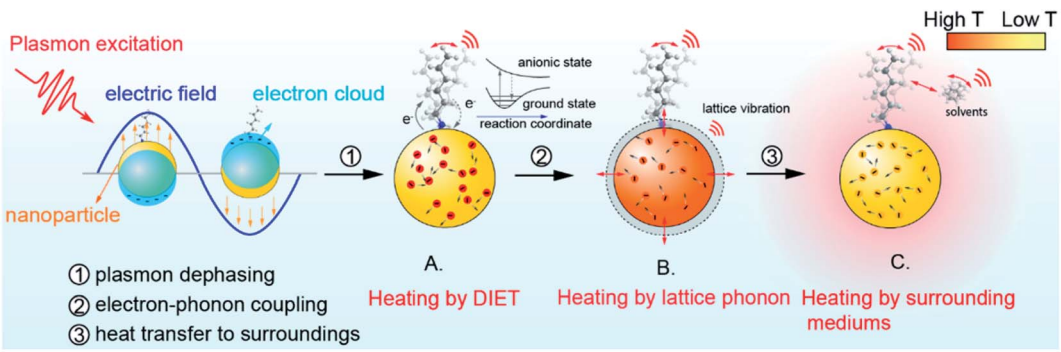

Scheme 1 Key photophysical processes of plasmonic photocatalysts and possible ways of heating surface adsorbates. Reproduced with permission from ref. 127. Copyright 2021, American Chemical Society.

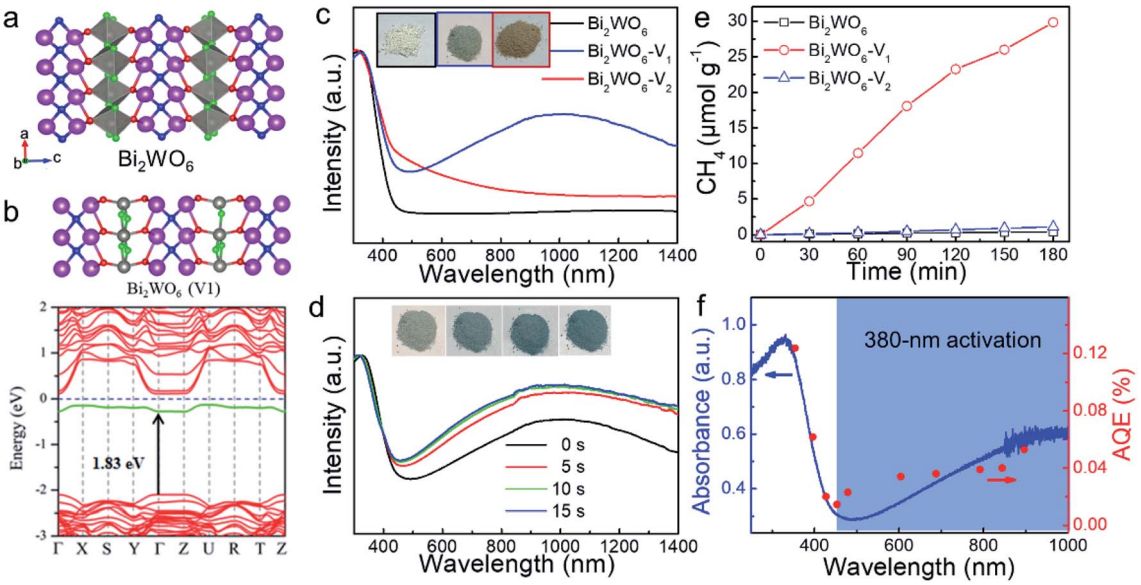

Fig. 11 Crystal structure (a) and DFT-calculated band structure (b) of Bi_2WO_6 with oxygen vacancies on W–O–W sites. UV-vis-NIR diffuse reflectance spectra and color images (c) of different samples Bi_2WO_6 (left), Bi_2WO_6–V_1 (middle) and Bi_2WO_6–V_2 (right). UV-vis-NIR reflectance spectra and color images (d) of plasmonic Bi_2WO_6–V1 with UV-visible light irradiation if different time 0, 5, 10, 15 s from left to right. CH_4 generation (e) over different samples Bi_2WO_6, Bi_2WO_6–V1 and Bi_2WO_6–V_2 under UV-Vis light irradiation, and the apparent quantum efficiency (AQE) of Bi_2WO_6–V1 (f) with 380 nm activation during CO_2 reduction reaction. Reproduced with permission from ref. 97. Copyright 2019, American Chemical Society.

phonon (defect)-assisted scattering within the bulk of TiN core; (iii) a secondary fraction of hot carriers (η_{inj}) at or near TiN surface are injected into the TiO_2 layer, with remaining carriers backscattered into the TiN core. The hot electron injection efficiency in TiN–TiO_2 NPs was measured to be 1.54%, consistent with the theoretical calculation of 1.5%.[70] Venkatesan *et al.* reported $MNbO_3$ (M = Ca, Sr, Ba) with N of 10^{22} cm^{-3} as a new family of noble metal-free plasmonic photocatalysts for hydrogen generation. The carrier decay kinetic studies demonstrated that the weak electron–phonon coupling effect on $CaNbO_3$ and $SrNbO_3$ allows the hot carrier to have enough time for migrating to the surface to drive the reaction, exhibiting superior performance than $BaNbO_3$ in photocatalysis.[128] Metal-free plasmonic boron phosphide/graphic carbon nitride (BP@C_3N_4) were found to exhibit broadband adsorption in the UV-Vis-NIR region and show enhanced activity for hydrogen generation, much higher than that of Pt–C_3N_4. The hot electron transfer (HET) from BP with LSPR to C_3N_4 was proposed as the possible mechanism.[129] Recently, Bi_2O_{3-x} with abundant oxygen vacancies has been synthesized on commercial bismuth powders by calcination in atmospheres exhibiting LSPR in the wavelength range of 600–1400 nm. The LSPR and oxygen

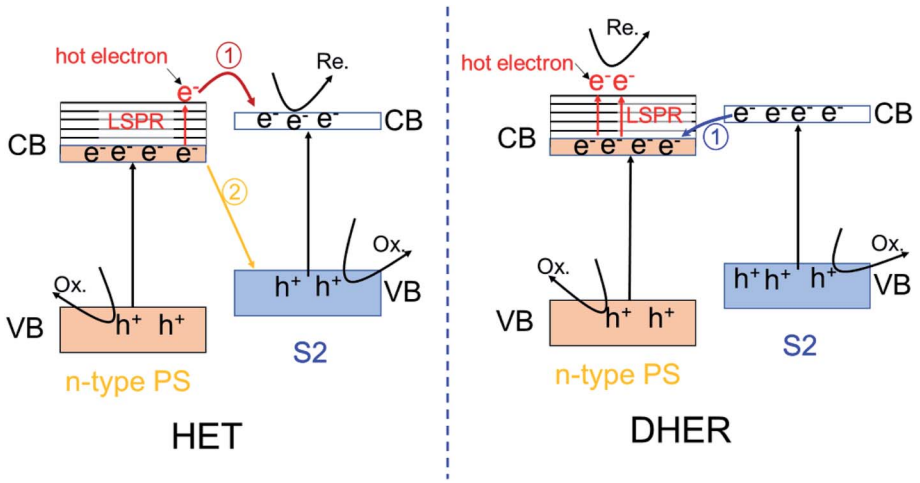

Scheme 2 Two possible photocatalytic mechanisms for n-type plasmonic semiconductor (PS) heterostructures: (1) hot electron transfer (HET) and (2) direct hot-electron reaction (DHER). S2: the other semiconductor, Re.: reduction, Ox.: oxidation.

vacancies were demonstrated to play critical roles in CO_2 reduction, achieving CO generation with the apparent quantum yield of 0.113% at 940 nm, 4-fold higher than that at 450 nm.[62]

Various studies have demonstrated that constructing abundant oxygen vacancies is one efficient strategy to increase the free carrier density of metal oxides for LSPR. Lou *et al.* extended this method to more complex crystal structures of Bi_2WO_6, in which three types of oxygen atoms exist as W–O–W, Bi–O–Bi and Bi–O–W (Fig. 11). Theoretically-simulated electronic structures of Bi_2WO_6 with three different oxygen vacancies demonstrated that the oxygen vacancies located on W–O–W sites induce one new localized electronic state close to CB.[97] The results imply the possibility of electron accumulations on the state for high carrier density and LSPR. With the above assumption, three Bi_2WO_6 samples with different oxygen vacancies were synthesized, and Bi_2WO_6–V1 with oxygen vacancy on W–O–W sites exhibited LSPR features in the UV-vis-NIR region. Both experimental and theoretical results on photocatalytic CO_2 reduction over Bi_2WO_6–V1 demonstrated that the LSPR and oxygen vacancy on W–O–W sites facilitate CH_4 generation.[97] Therefore, inducing oxygen vacancy around metal ions with valence changes is one possible strategy to construct LSPR on semiconductors for photocatalysis.

4. Conclusion and outlook

As discussed in the above sections, LSPR of semiconductor NCs is unique optical property, which is mainly determined by the free carrier density and influenced by various physical parameters including particle size, shape, surface depletion layers and the surrounding medium. However, in contrast to metal NPs, plasmonic semiconductor NCs can be classified as n-type and p-type by their free charges of electrons on CB or holes on VB. Most importantly, the surface of plasmonic semiconductors is more complex than that of metals, and a depletion layer formed by dramatically decreasing carrier density lowers the sensitivity of plasmonic semiconductors to the surrounding medium and weakens the dipole–dipole interaction between plasmonic semiconductor NCs. The charge effective mass (m_e) in semiconductors is dependent on crystal lattices, which may results in anisotropic LSPR properties along with different crystal directions. The carrier densities of various plasmonic semiconductors reported are mostly calculated by numerical simulation using the Drude model. However, the results may be more precise through experimental measurements because the doping process will induce changes in intrinsic dielectric properties of semiconductors, which is always neglected in the Drude model calculation. Until now, plasmonic semiconductors reported for plasmon-enhanced photocatalysis are mostly focused on doped tungsten oxides, molybdenum oxides and copper chalcogenides, which have free carrier density of 10^{21} to 10^{22} cm^{-3} for LSPR in Vis-NIR, boosting photocatalytic hydrogen generation, organic pollution degradation, organic synthesis and CO_2 reduction. Plasmonic hot carrier generation is considered to play a critical role in photocatalysis, but the detailed mechanism is still unclear. For n-type plasmonic semiconductors, two possible mechanisms were proposed as described in Scheme 2. One is the hot-electron transfer (HET), similar to DET of plasmonic metal/semiconductors, in which hot-electron generated on a plasmonic semiconductor can be transferred to the CB (1, left) of other semiconductors for the reduction reaction, or transfer to the VB (2, left) as Z-scheme structure promoting photo charge separation for photocatalysis. The other possible mechanism is a direct hot-electron reaction (DHER), in which the plasmonic semiconductor generates hot electrons for photocatalysis on the surface, and the photoelectron injection from intrinsic VB or from the CB of the other semiconductor (1, right) in the heterostructure, boosting hot electron generation for photocatalysis. For p-type plasmonic semiconductors, the fast plasmonic heating process was studied by ultrafast optical spectroscopy, but the detailed mechanisms of plasmonic hot carrier generation and transfer are still unclear. The different roles of hot electron and hot holes in photocatalysis are also quite necessary to be investigated in the future.

From the fundamental of LSPR on semiconductors, the possible strategies to improve photocatalysis of plasmonic semiconductors are predicted in this perspective as follows:

4.1 Decreasing the thickness of depletion layers

The dramatically decreasing of carrier density on the surface of the semiconductor forms the insulated shell allowing the incident light pass to occur oscillation with free carriers for LSPR, however, it strongly restricts the hot electron transfer from the surface to outside leading to fast recombination. Therefore, decreasing the thickness or removing the depletion layers could greatly promote hot electron generation and transfer, facilitating hot carriers separation for photocatalysis.

4.2 Constructing plasmonic p–n heterostructures

The n-type plasmonic semiconductor can generate hot electrons in the CB for photo-reduction, and the p-type plasmonic semiconductor can generate hot holes in the VB for photo-oxidation. Constructing p–n heterostructures is one promising strategy to promote charge accumulation on different parts, in which the intrinsic band gap excitation generates electrons in CB of n-type plasmonic semiconductors and holes on VB of p-type ones for enhancing LSPR. Besides, by controlling the potential position of band structures, the electrons in the CB of p-type semiconductors can transfer to the CB of n-type ones and holes on VB of n-type semiconductors can transfer to VB of p-type ones, leading to high and stable carrier densities on both of n- and p-type semiconductors for strong LSPR. Therefore, it is a potential strategy to construct high-active plasmonic semiconductor heterostructures for photocatalysis.

4.3 Anisotropic LSPR on semiconductors

In contrast to plasmonic metals, the high-frequency permittivity, damping and the charge effective mass in semiconductors are highly dependent on crystal lattice directions. Increasing charge density and synthesizing anisotropic microstructures are one possible strategies to construct strong LSPR on semiconductors for enhancing photocatalysis.

4.4 Mechanism study on p-type plasmonic semiconductor for photocatalysis

Compared to the possible mechanisms of HET and DHER on n-type plasmonic semiconductor photocatalysts, it is still unclear for that of p-type plasmonic semiconductors. An in-depth understanding of the photo-chemical and -physical process of hot carrier generation, transfer and recombination on p-type plasmonic semiconductors will be greatly helpful for the development of high-active plasmonic photocatalysts in the future.

Apart from photocatalysis, semiconductor NCs can also hold great promise in other applications such as fluorescence enhancement, SERS, optical detection, and photothermal applications.[71,72,74,130–133] For example, the potential of plasmonic semiconductors to enhance upconversion luminescence (UCL) has been explored. Li *et al.* reported over 500-fold selective UCL enhancement at the green emission of $NaYF_4$:Yb^{3+}, Er^{3+} upconversion NPs achieved by plasmonic WO_{3-x}, which is larger than those of most reported metallic nanostructures.[72] Such significant UCL selective enhancement is mainly ascribed to plasmonic WO_{3-x} induced intense electrical field and photothermal effect. Plasmonic semiconductors with an intense electromagnetic field have also been explored for surface-enhanced Raman scattering (SERS) active substrates. In addition to electromagnetic mechanisms, specific binding properties of target molecules also play important role in determining SERS signal strength. In this sense, plasmonic semiconductors are expected to complement conventional metal-based SERS substrates since the surface chemical bonding with analytes is quite distinct for metal oxides/chalcogenides and metals. Recently, plasmonic MoO_3 nanocubes aligned on graphene oxide have been reported as the SERS substrate for sensitive detection of norovirus resulting from the combined electromagnetic and chemical mechanisms.[130] Moreover, the LSPR-induced photothermal effect makes plasmonic semiconductors promising candidates for photoacoustic imaging, photothermal therapy and more.[74,131–133] As the plasmon energy of plasmonic semiconductor NCs does not strongly depend on size, they can be synthesized into small sizes with LSPR in the IR region of the biological transparency window, and thus are promising for biomedical applications. Novel dopamine enveloped WO_{3-x} nanodots have been successfully synthesized as a multifunctional therapeutic nanoplatform to trigger synergistic photothermal/photodynamic therapy for solid tumor ablation *in vivo* without damaging healthy tissues under 808 nm NIR irradiation.[133]

To date, plasmonic semiconductor NCs with near-field enhancement, high absorption cross-section, hot carrier generation, the photothermal effect and the ability to construct complex nanostructures have demonstrated great feasibility for a wide range of applications that are not restricted to photocatalysis. Although there has been considerable progress made in understanding LSPR in semiconductor NCs and its related applications, there remains much theoretical and experimental work that needs to be done.

Conflicts of interest

There are no conflicts to declare.

Acknowledgements

This work was supported by the National Natural Science Foundation of China (No. 51872125, 11904133), Guangdong Natural Science Funds for Distinguished Young Scholar (2018B030306004) and GDUPS (2018), the Fundamental Research Funds for the Central Universities (No. 21619322) and Regional Joint Foundation in Guangdong Province (No. 2019A1515110210).

References

1 K. M. Mayer and J. H. Hafner, *Chem. Rev.*, 2011, **111**, 3828–3857.
2 I. Jung, M. Kim, M. Kwak, G. Kim, M. Jang, S. M. Kim, D. J. Park and S. Park, *Nat. Commun.*, 2018, **9**, 1010.
3 D. B. Li, X. J. Sun, Y. P. Jia, M. I Stockman, H. P. Paudel, H. Song, H. Jiang and Z. M. Li, *Light: Sci. Appl.*, 2017, **6**, e17038.
4 T. Umakoshi, M. Tanaka, Y. Saito and P. Verma, *Sci. Adv.*, 2020, **6**, eaba4179.
5 J. C. Tong, W. Zhou, Y. Qu, Z. J. Xu, Z. M. Huang and D. H. Zhang, *Nat. Commun.*, 2017, **8**, 1660.
6 J. A. Jackman, A. R. Ferhan and N. J. Cho, *Chem. Soc. Rev.*, 2017, **46**, 3615–3660.
7 A. Loiseau, L. Zhang, D. Hu, M. Salmain, Y. Mazouzi, R. Flack, B. Liedberg and S. Boujday, *ACS Appl. Mater. Interfaces*, 2019, **11**, 46462–46471.
8 Y. J. Hu, X. Y. Liu, Z. W. Cai, H. Zhang, H. Gao, W. J. He, P. Wu, C. X. Cai, J. J. Zhu and Z. J. Yan, *Chem. Mater.*, 2019, **31**, 471–482.
9 C. Tao, L. An, J. Lin, Q. Tian and S. Yang, *Small*, 2019, **15**, 1903473.
10 Y. C. Chen, Y. S. Huang, H. Huang, P. J. Su, T. P. Perng and L. J. Chen, *Nano Energy*, 2020, **67**, 104225.
11 M. Dhiman, *J. Mater. Chem. A*, 2020, **8**, 10074–10095.
12 K. Awazu, M. Fujimaki, C. Rockstuhl, J. Tominaga, H. Murakami, Y. Ohki, N. Yoshida and T. Watanabe, *J. Am. Chem. Soc.*, 2008, **130**, 1676–1680.
13 X. Chen, H. Y. Zhu, J. C. Zhao, Z. F. Zheng and X. P. Gao, *Angew. Chem.*, 2008, **120**, 5433–5436.
14 D. A. Panayotov, A. I. Frenkel and J. R. Morris, *ACS Energy Lett*, 2017, **2**, 1223–1231.
15 P. Wang, B. Huang, X. Qin, X. Zhang, Y. Dai, J. Wei and M. H. Whangbo, *Angew. Chem., Int. Ed.*, 2008, **47**, 7931–7933.
16 A. Tanaka, K. Teramura, S. Hosokawa, H. Kominami and T. Tanaka, *Chem. Sci.*, 2017, **8**, 2574–2580.
17 L. H. Yu, Y. Shao and D. Z. Li, *Appl. Catal., B*, 2017, **204**, 216–223.
18 R. Shi, Y. H. Cao, Y. J. Bao, Y. F. Zhao, G. I. N. Waterhouse, Z. Y. Fang, L. Z. Wu, C. H. Tung, Y. D. Yin and T. R. Zhang, *Adv. Mater.*, 2017, **29**, 1700803.

19 J. R. Liu, J. D. Li, F. Wei, X. L. Zhao, Y. C. Su and X. J. Han, *ACS Sustainable Chem. Eng.*, 2019, **7**, 11258–11266.
20 R. Zhang, M. Hummelgård, J. Örtegren, Y. Yang, H. Andersson, E. Balliu, N. Blomquist, M. Engholm, M. Olsen, Z. L. Wang and H. Olina, *Nano Energy*, 2019, **63**, 103842.
21 X. C. Ma, Y. Dai, L. Yu and B. B. Huang, *Light: Sci. Appl.*, 2016, **5**, 16017.
22 Z. Lou, Z. Wang, B. Huang and Y. Dai, *ChemCatChem*, 2014, **6**, 2456–2476.
23 Y. B. Lou, Y. K. Zhang, L. Cheng, J. X. Chen and Y. X. Zhao, *ChemSusChem*, 2018, **11**, 1505–1511.
24 B. Wu, D. Liu, S. Mubeen, T. T. Chuong, M. Moskovits and G. D. Stucky, *J. Am. Chem. Soc.*, 2016, **138**, 1114–1117.
25 L. Ma, K. Chen, F. Nan, J. H. Wang, D. J. Yang, L. Zhou and Q. Q. Wang, *Adv. Funct. Mater.*, 2016, **26**, 6076–6083.
26 Z. Lou, S. Kim, M. Fujitsuka, X. Yang, B. Li and T. Majima, *Adv. Funct. Mater.*, 2018, **28**, 1706969.
27 Y. Liu, Q. Chen, D. A. Cullen, Z. Xie and T. Lian, *Nano Lett.*, 2020, **20**, 4322–4329.
28 J. Xue, O. Elbanna, S. Kim, M. Fujitsuka and T. Majima, *Chem. Commun.*, 2018, **54**, 6052–6055.
29 C. Y. Zhang, F. C. Jia, Z. Y. Li, X. Huang and G. Lu, *Nano Res.*, 2020, **13**, 3183–3197.
30 Z. Zheng, T. Tachikawa and T. Majima, *J. Am. Chem. Soc.*, 2014, **136**, 6870–6873.
31 Z. Zheng, T. Tachikawa and T. Majima, *J. Am. Chem. Soc.*, 2015, **137**, 948–957.
32 Z. Lou, M. Fujitsuka and T. Majima, *ACS Nano*, 2016, **10**, 6299–6305.
33 Z. Lou, S. Kim, P. Zhang, X. Shi, M. Fujitsuka and T. Majima, *ACS Nano*, 2017, **11**, 968–974.
34 G. Chen, M. Sun, J. Li, M. Zhu, Z. Lou and B. Li, *Nanoscale*, 2019, **11**, 18874–18880.
35 Z. Lou, M. Fujitsuka and T. Majima, *J. Phys. Chem. Lett.*, 2017, **8**, 844–849.
36 A. Agrawal, S. H. Cho, O. Zandi, S. Ghosh, R. W. Johns and D. J. Milliron, *Chem. Rev.*, 2018, **118**, 3121–3207.
37 Y. N. Ji, W. Xu, D. Y. Li, D. L. Zhou, X. Chen, N. Ding, J. Li, N. Wang, X. Bai and H. W. Song, *Nano Energy*, 2019, **61**, 211–220.
38 C. Lan, Z. Shi, R. Cao, C. Li and H. Zhang, *Nanoscale*, 2020, **12**, 11784–11807.
39 H. B. Yin, Y. Kuwahara, K. Mori, C. Louis and H. Yamashita, *Catal. Sci. Technol.*, 2020, **10**, 4141–4163.
40 X. W. Zhang, S. M. Liu, D. Z. Tan, Y. H. Xian, D. D. Zhang, Z. X. Zhang, Y. Liu, X. F. Liu and J. R. Qiu, *Chem. Mater.*, 2020, **32**, 3180–3187.
41 S. Long, X. Cao, R. Huang, F. Xu, N. Li, A. Huang, G. Sun, S. Bao, H. Luo and P. Jin, *ACS Appl. Mater. Interfaces*, 2019, **11**(25), 22692–22702.
42 H. Cheng, T. Kamegawa, K. Mori and H. Yamashita, *Angew. Chem., Int. Ed.*, 2014, **53**, 2910–2914.
43 H. Cheng, M. Wen, X. Ma, Y. Kuwahara, K. Mori, Y. Dai, B. Huang and H. Yamashita, *J. Am. Chem. Soc.*, 2016, **138**, 9316–9324.
44 H. Cheng, X. Qian, Y. Kuwahara, K. Mori and H. Yamashita, *Adv. Mater.*, 2015, **27**, 4616–4621.
45 H. Yin, Y. Kuwahara, K. Mori, H. Cheng, M. Wen, Y. Huo and H. Yamashita, *J. Phys. Chem. C*, 2017, **121**, 23531–23540.
46 Z. Lou, Q. Gu, L. Xu, Y. Liao and C. Xue, *Chem. Asian. J.*, 2015, **10**, 1291–1294.
47 Z. Lou, Q. Gu, Y. Liao, S. Yu and C. Xue, *Appl. Catal., B*, 2016, **184**, 258–263.
48 Z. Zhang, J. Huang, Y. Fang, M. Zhang, K. Liu and B. Dong, *Adv. Mater.*, 2017, **29**, 1606688.
49 Z. Lou, M. Zhua, X. Yang, Y. Zhang, M. H. Whangbo, B. Li and B. Huang, *Appl. Catal., B*, 2018, **226**, 10–15.
50 Z. Lou, P. Zhang, J. Li, X. Yang, B. Huang and B. Li, *Adv. Funct. Mater.*, 2019, **29**, 1808696.
51 J. Li, X. Xu, B. Huang, Z. Lou and B. Li, *ACS Appl. Mater. Interfaces*, 2021, **13**, 10047–10053.
52 L. Liu, B. Zhou, L. Deng, W. Fu, J. Zhang, M. Wu, W. Zhang, B. Zou and H. Zhong, *J. Phys. Chem. C*, 2014, **118**, 26964–26972.
53 Y. Liu, M. Liu and M. T. Swihart, *J. Phys. Chem. C*, 2017, **121**, 13435–13447.
54 N. Ghorai and H. N. Ghosh, *J. Phys. Chem. C*, 2019, **123**, 28401–28410.
55 J. M. Luther, P. K. Jain, T. Ewers and A. P. Alivisatos, *Nat. Mater.*, 2011, **10**, 361–366.
56 L. W. Chou, N. Shin, S. V. Sivaram and M. A. Filler, *J. Am. Chem. Soc.*, 2012, **134**, 16155–16158.
57 Z. K. Liu, Y. X. Zhong, I. Shafei, R. Borman, S. Jeong, J. Chen, Y. Losovyj, X. F. Gao, N. Li, Y. P. Du, E. Sarnello, T. Li, D. Su, W. L. Ma and X. C. Ye, *Nat. Commun.*, 2019, **10**, 1394.
58 N. Li, X. Cao, Y. Li, T. Chang, S. Long, Y. Zhou, G. Sun, L. Ge and P. Jin, *Chem. Commun.*, 2018, **54**, 5241–5244.
59 A. H. Odda, Y. Xu, J. Lin, G. Wang, N. Ullah, A. Zeb, K. Liang, L. Wen and A. W. Xu, *J. Mater. Chem. B*, 2019, **7**, 2032–2042.
60 B. Tandon, S. Ghosh and D. J. Milliron, *Chem. Mater.*, 2019, **31**, 7752–7760.
61 R. Giannuzzi, F. D. Donato, L. D. Trizio, A. G. Monteduro, G. Maruccio, R. Scarfiello, A. Qualtieri and L. Manna, *ACS Appl. Mater. Interfaces*, 2019, **11**(43), 39921–39929.
62 Y. Li, M. Wen, Y. Wang, G. Tian, C. Wang and J. Zhao, *Angew. Chem. Int. Ed.*, 2021, **60**, 910–916.
63 R. M. C. Castro, M. Casavola, M. Schilfgaarde, A. V. Krasavin, M. A. Green, D. Richards and A. V. Zayats, *ACS Nano*, 2019, **13**(6), 6550–6560.
64 L. Ma, D. J. Yang, X. P. Song, H. X. Li, S. J. Ding, L. Xiong, P. L. Qin and X. B. Chen, *Sol. RRL.*, 2020, **4**, 1900376.
65 G. Shen and P. G. Sionnest, *J. Phys. Chem. C*, 2016, **120**(21), 11744–11753.
66 X. Tang, G. Wu and K. W. C. Lai, *J. Mater. Chem. C*, 2017, **5**, 362–369.
67 M. P. Fischer, A. Riede, K. Gallacher, J. Frigerio, G. Pellegrini, M. Ortolani, D. J. Paul, G. Isella, A. Leitenstorfer, P. Biagioni and D. Brida, *Light: Sci. Appl.*, 2018, **7**, 106.

68 I. R. Howell, B. Giroire, A. Garcia, S. Li, C. Aymonier and J. J. Watkins, *J. Mater. Chem. C*, 2018, **6**, 1399–1406.
69 S. Askari, D. Mariotti, J. E. Stehr, J. Benedikt, J. Keraudy and U. Helmersson, *Nano Lett.*, 2018, **18**(9), 5681–5687.
70 X. Xu, A. Dutta, J. Khurgin, A. Wei, V. M. Shalaev and A. Boltasseva, *Laser Photonics Rev.*, 2020, **14**, 1900376.
71 P. Li, L. Zhu, C. Ma, L. Zhang, L. Guo, Y. Liu, H. Ma and B. Zhao, *ACS Appl. Mater. Interfaces*, 2020, **12**, 19153–19160.
72 J. Li, W. Zhang, C. Lu, Z. Lou and B. Li, *Nanoscale Horiz.*, 2019, **4**, 999–1005.
73 D. Wan, B. Yan, J. Chen, S. Wu, J. Hong, D. Song, X. Zhao, X. Chi, S. Zeng, Z. Huang, C. Li, K. Han, W. Zhou, Y. Cao, A. Rusydi, S. J. Pennycook, P. Yang, A. Ariando, R. Xu, Q. H. Xu, X. R. Wang and T. Venkatesan, *Chem. Mater.*, 2019, **31**, 2320–2327.
74 W. Xua, H. C. Liu, D. L. Zhou, X. Chen, N. Ding, H. W. Song and H. Ågren, *Nano Today*, 2020, **33**, 100892.
75 L. H. Chen, H. F. Hu, Y. Z. Chen, Y. Li, J. Gao and G. H. Li, *Chem. –Eur. J.*, 2021, **27**, 1057–1065.
76 S. Cong, Y. Yuan, Z. Chen, J. Hou, M. Yang, Y. Su, Y. Zhang, L. Li, Q. Li, F. Geng and Z. Zhao, *Nat. Commun.*, 2015, **6**, 7800.
77 M. Remškar, J. Kovac, M. Viršek, M. Mrak, A. Jesih and A. Seabaugh, *Adv. Funct. Mater.*, 2007, **17**, 1974–1978.
78 H. Cheng, M. Klapproth, A. Sagaltchik, S. Li and A. Thomas, *J. Mater. Chem. A.*, 2018, **6**, 2249–2256.
79 H. Zheng, J. Z. Ou, M. S. Strano, R. B. Kaner, A. Mitchell and K. Kalantar-zadeh, *Adv. Funct. Mater.*, 2011, **21**, 2175–2196.
80 K. Manthiram and A. P. Alivisatos, *J. Am. Chem. Soc.*, 2012, **134**, 3995–3998.
81 G. Prusty, J. T. Lee, S. Seifert, B. B. Muhoberac and R. Sardar, *J. Am. Chem. Soc.*, 2020, **142**, 5938–5942.
82 X. Zhang, X. Wang, X. Yi, L. Liu, J. Ye and D. Wang, *ACS Appl. Energy Mater.*, 2020, **3**, 3569–3576.
83 Y. Li, J. Cheng, Y. Liu, P. Liu, W. Cao, T. He, R. Chen and Z. Tang, *J. Phys. Chem. C*, 2017, **121**, 5208–5214.
84 I. Kriegel, C. Jiang, J. R. Fernández, R. D. Schaller, D. V. Talapin, E. Como and J. Feldmann, *J. Am. Chem. Soc.*, 2012, **134**, 1583–1590.
85 L. Liu, H. Zhong, Z. Bai, T. Zhang, W. Fu, L. Shi, H. Xie, L. Deng and B. Zou, *Chem. Mater.*, 2013, **25**, 4828–4834.
86 R. Alam, M. Labine, C. J. Karwacki and P. V. Kamat, *ACS Nano*, 2016, **10**, 2880–2886.
87 L. J. E. Anderson, K. M. Mayer, R. D. Fraleigh, Y. Yang, S. Lee and J. H. Hafner, *J. Phys. Chem. C*, 2010, **114**, 11127–11132.
88 W. Ni, X. Kou, Z. Yang and J. Wang, *ACS Nano*, 2008, **2**, 677–686.
89 S. W. Hsu, W. Bryks and A. R. Tao, *Chem. Mater.*, 2012, **24**, 3765–3771.
90 S. W. Hsu, C. Ngo and A. R. Tao, *Nano Lett.*, 2014, **14**, 2372–2380.
91 T. M. Mattox, A. Bergerud, A. Agrawal and D. J. Milliron, *Chem. Mater.*, 2014, **26**, 1779–1784.
92 J. Kim, A. Agrawal, F. Krieg, A. Bergerud and D. J. Milliron, *Nano Lett.*, 2016, **16**, 3879–3884.
93 F. Wang, Q. Li, L. Lin, H. Peng, Z. Liu and D. Xu, *J. Am. Chem. Soc.*, 2015, **137**, 12006–12012.
94 O. Zandi, A. Agrawal, A. B. Shearer, L. C. Reimnitz, C. J. Dahlman, C. M. Staller and D. J. Milliron, *Nat. Mater.*, 2018, **17**, 710–717.
95 S. L. Gibbs, C. M. Staller and D. J. Milliron, *Acc. Chem. Res.*, 2019, **52**, 2516–2524.
96 S. Q. Luo, X. H. Ren, H. W. Lin, H. Song and J. H. Ye, *Chem. Sci.*, 2021, **12**, 5701–5719.
97 C. Lu, X. Li, Q. Wu, J. Li, L. Wen, Y. Dai, B. Huang, B. Li and Z. Lou, *ACS Nano*, 2021, **15**, 3529–3539.
98 H. Yin, Y. Kuwahara, K. Mori, H. Cheng, M. Wen and H. Yamashita, *J. Mater. Chem. A.*, 2017, **5**, 8946–8953.
99 Z. Zhang, X. Jiang, B. Liu, L. Guo, N. Lu, L. Wang, J. Huang, K. Liu and B. Dong, *Adv. Mater.*, 2018, **30**, 1705221.
100 N. Lu, Z. Zhang, Y. Wang, B. Liu, L. Guo, L. Wang, J. Huang, K. Liu and B. Dong, *Appl. Catal., B*, 2018, **233**, 19–25.
101 Y. Yang, Y. Cong, B. Cao, Y. Xiao, J. Shang, Y. Tong, H. Zhang, Y. Liu, B. Dong and J. H. Zhang, *Nanotechnology*, 2020, **31**, 165707.
102 Z. Zhang, Y. Liu, Y. Fang, B. Cao, J. Huang, K. Liu and B. Dong, *Adv. Sci.*, 2018, **5**, 1800748.
103 Y. Liu, Z. Zhang, Y. Fang, B. Liu, J. Huang, F. Miao, Y. Bao and B. Dong, *Appl. Catal., B*, 2019, **252**, 164–173.
104 J. Shang, X. Xu, K. Liu, Y. Bao, Y. Yang and M. He, *Ceram. Int.*, 2019, **45**, 16625–16630.
105 P. Du, Y. Wei, J. Sun, Z. Ying, J. Wu and N. Xu, *J. Phys. Chem. C*, 2021, **125**, 4205–4210.
106 Y. Z. Zhang, B. Q. Xia, J. R. Ran, K. Davey and S. Z. Qiao, *Adv. Energy Mater.*, 2020, **10**, 1903879.
107 C. Lu, J. Li, G. Chen, B. Li and Z. Lou, *Nanoscale*, 2019, **11**, 12774–12780.
108 J. Li, G. Chen, J. Yan, B. Huang, H. Cheng, Z. Lou and B. Li, *Appl. Catal., B*, 2020, **264**, 118517.
109 C. Lu, J. Li, J. Yan, B. Li, B. Huang and Z. Lou, *Appl. Mater. Today*, 2020, **20**, 100744.
110 D. Spetter, M. N. Tahir, J. Hilgert, I. Khan, A. Qurashi, H. Lu, T. Weidner and W. Tremel, *ACS Sustainable Chem. Eng.*, 2018, **6**, 12641–12649.
111 H. Wu, X. Li, Y. Cheng, Y. Xiao, R. Li, Q. Wu, H. Lin, J. Xu, G. Wang, C. Lin, X. Chen and Y. Wang, *J. Mater. Chem. A*, 2020, **8**, 2827.
112 X. Wu, S. Yin, D. Xue, S. Komarneni and T. Sato, *Nanoscale*, 2015, **7**, 17048–17054.
113 H. Man, C. Wang, Y. Sun, Y. Ning, P. Song and W. Huang, *J. Materiomics.*, 2016, **2**, 338–343.
114 J. Yang, J. Liu, Y. Qiao, F. Shi, S. Ran, Y. Dong and S. Liu, *CrystEngComm*, 2020, **22**, 573–586.
115 Y. Li, X. Wu, J. Li, K. Wang and G. Zhang, *Appl. Catal., B*, 2018, **229**, 218–226.
116 S. Sun, D. Deng, C. Kong, X. Song and Z. Yang, *Dalton Trans.*, 2012, **41**, 3214–3222.
117 L. N. Qiao, H. C. Wang, Y. Shen, Y. H. Lin and C. W. Nan, *Nanomaterials*, 2017, **7**, 19.
118 H. Gao, Y. Chen, H. Li, F. Zhang and G. Tian, *Chem. Eng. J.*, 2019, **363**, 247–258.
119 X. Liu, Q. Liu, P. Wang, Y. Liu, B. Huang, E. A. Rozhkova, Q. Zhang, Z. Wang, Y. Dai and J. Lu, *Chem. Eng. J.*, 2018, **337**, 480–487.

120 Z. Liu, X. Liu, X. Gu, R. Guo and W. Zhong, *Nanoscale Res. Lett.*, 2019, **14**, 95.
121 L. Zhou, Z. Liu, Z. Guan, B. Tian, L. Wang, Y. Zhou, Y. Zhou, J. Lei, J. Zhang and Y. Liu, *Appl. Catal., B*, 2020, **263**, 118326.
122 L. Jiang, K. Wang, X. Wu and G. Zhang, *Solar RRl*, 2020, **5**, 2000326.
123 X. Shao, T. Zhang, B. Li, Y. Wu, X. Ma, J. Wang and S. Jiang, *CrystEngComm*, 2020, **22**, 678–685.
124 X. Y. Gan, E. L. Keller, C. L. Warkentin, S. E. Crawford, R. R. Frontiera and J. E. Millstone, *Nano Lett.*, 2019, **19**, 2384–2388.
125 P. H. Liu, M. Wen, C. S. Tan, M. N. García, Y. Kuwahara, K. Mori, H. Yamashita and L. J. Chen, *Nano Energy*, 2017, **31**, 57–63.
126 S. Ma, K. Chen, Y. H. Qiu, L. L. Gong, G. M. Pan, Y. J. Lin, Z. H. Hao, L. Zhou and Q. Q. Wang, *J. Mater. Chem. A*, 2019, **7**, 3408–3414.
127 W. Yang, Y. Liu, J. R. McBride and T. Lian, *Nano Lett.*, 2021, **21**, 453–461.
128 D. Wan, B. Yan, J. Chen, S. Wu, J. Hong, D. Song, X. Zhao, X. Chi, S. Zeng, Z. Huang, C. Li, K. Han, W. Zhou, Y. Cao, A. Rusydi, S. J. Pennycook, P. Yang, A. Ariando, R. Xu, Q. H. Xu, X. R. Wang and T. Venkatesan, *Chem. Mater.*, 2019, **31**, 2320–2327.
129 B. Tian, Y. Q. Wu and G. X. Lu, *Appl. Catal., B*, 2021, **280**, 119410.
130 O. J. Achadu, F. Abe, T. Suzuki and E. Y. Park, *ACS Appl. Mater. Interfaces*, 2020, **12**, 43522–43534.
131 Y. Mantri and J. V. Jokerst, *ACS Nano*, 2020, **14**, 9408–9422.
132 H. Zhu, Y. Wang, C. Chen, M. R. Ma, J. F. Zeng, S. Z. Li, Y. S. Xia and M. Y. Gao, *ACS Nano*, 2017, **11**, 8273–8281.
133 J. P. Sheng, L. Zhang, L. Deng, Y. J. Han, L. Q. Wang, H. C. He and Y. N. Liu, *Chem. Eng. J.*, 2020, **383**, 123071.
134 X. J. Tan, L. Z. Wang, C. Cheng, X. F. Yan, B. Shen and J. L. Zhang, *Chem. Comm.*, 2016, **52**, 2893–2896.
135 D. X. Zhu, L. J. Wang, Z. M. Liu and A. W. Tang, *Appl. Surf. Sci.*, 2020, **509**, 145327.
136 R. J. Mendelsberg, G. Garcia, H. B. Li, L. Manna and D. J. Milliron, *J. Phys. Chem. C*, 2012, **116**, 12226–12231.
137 S. H. Cho, K. M Roccapriore, C. K. Dass, S. Ghosh, J. Choi, J. Noh, L. C Reimnitz, S. Heo, K. Kim, K. Xie, B. A. Korgel, X. Q. Li, J. R Hendrickson, J. A. Hachtel and D. J Milliron, *J. Chem. Phys.*, 2020, **152**, 014709.
138 E. L. Runnerstrom, A. Bergerud, A. Agrawal, R. W. Johns, C. J. Dahlman, A. Singh, S. M. Selbach and D. J. Milliron, *Nano Lett.*, 2016, **16**, 3390–3398.
139 A. K. Guria and N. Pradhan, *Chem. Mater.*, 2017, **29**, 9360–9368.
140 X. C. Ye, J. Y. Fei, B. T. Diroll, T. Paik and C. B. Murray, *J. Am. Chem. Soc.*, 2014, **136**, 11680–11686.
141 A. Calzolari, A. Ruini and A. Catellani, *ACS Photonics*, 2014, **1**, 703–709.
142 S. Ghosh, M. Saha, V. D. Ashok, B. Dalal and S. K. De, *J. Phys. Chem. C*, 2015, **119**, 1180–1187.
143 S. Zhou, X. D. Pi, Z. Y. Ni, Y. Ding, Y. Y. Jiang, C. H. Jin, C. Delerue, D. R. Yang and T. Nozaki, *ACS Nano*, 2015, **9**(1), 378–386.
144 S. Cao, S. L. Zhang, T. R. Zhang, A. Fisher and J. Y. Lee, *J. Mater. Chem. C*, 2018, **6**, 4007.